

Structure-Guided Design of Potent Spirocyclic Inhibitors of Severe Acute Respiratory Syndrome Coronavirus-2 3C-like Protease

Chamandi S. Dampalla, Athri D. Rathnayake, Anushka C. Galasiti Kankanamalage, Yunjeong Kim, Krishani Dinali Perera, Harry Nhat Nguyen, Matthew J. Miller, Trent K. Madden, Hunter R. Picard, Hayden A. Thurman, Maithri M. Kashipathy, Lijun Liu, Kevin P. Battaile, Scott Lovell, Kyeong-Ok Chang,* and William C. Groutas*



Cite This: *J. Med. Chem.* 2022, 65, 7818–7832



Read Online

ACCESS |



Metrics & More



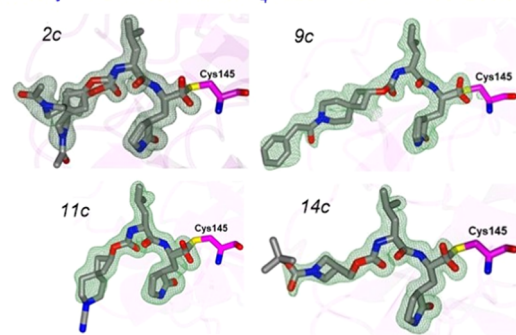
Article Recommendations



Supporting Information

ABSTRACT: The worldwide impact of the ongoing COVID-19 pandemic on public health has made imperative the discovery and development of direct-acting antivirals aimed at targeting viral and/or host targets. SARS-CoV-2 3C-like protease (3CL^{pro}) has emerged as a validated target for the discovery of SARS-CoV-2 therapeutics because of the pivotal role it plays in viral replication. We describe herein the structure-guided design of highly potent inhibitors of SARS-CoV-2 3CL^{pro} that incorporate in their structure novel spirocyclic design elements aimed at optimizing potency by accessing new chemical space. Inhibitors of both SARS-CoV-2 3CL^{pro} and MERS-CoV 3CL^{pro} that exhibit nM potency and high safety indices have been identified. The mechanism of action of the inhibitors and the structural determinants associated with binding were established using high-resolution cocrystal structures.

Diversity of Exit Vectors in the S₄ Subsite of SARS-CoV-2 3CL^{pro}



INTRODUCTION

Severe Acute Respiratory Syndrome coronavirus-2 (SARS-CoV-2), the causative agent of coronavirus disease (COVID-19), is an enveloped, single-stranded, positive-sense RNA β -coronavirus in the family Coronaviridae.^{1–3} SARS-CoV-2 infections are continuing to have a major impact on public health worldwide despite the availability of vaccines,^{4,5} and this is further exacerbated by the limited armamentarium of effective countermeasures that can be deployed to combat the virus, including emerging and reemerging strains, underscoring the urgent need for the development of small-molecule therapeutics and prophylactics.^{6–9}

The SARS-CoV-2 genome (~30 kb) encodes multiple structural (spike (S), envelope (E), membrane (M), and nucleocapsid (N)) and nonstructural proteins.^{1,10} The homotrimeric spike protein plays a critical role in viral attachment, fusion, and entry by binding to the receptor-binding domain of the host receptor (ACE2), followed by the furin-, transmembrane serine protease 2-, and cathepsin L-mediated fusion of viral and endosomal membranes, and the release of viral RNA into the cytosol.^{11–13} The replicase is expressed by two open reading frames that encode two large polyproteins (pp1a and pp1ab), which are processed by the 3C-like protease (3CL^{pro}) and papain-like protease (PL^{pro}), to generate mature structural and nonstructural proteins. The 3CL^{pro}, also called main protease (M^{pro}), is an induced-fit enzyme with an extended binding cleft, a Cys-His catalytic

dyad, and a primary substrate specificity for a P₁ Gln residue and a preference for a P₂ Leu.^{14,15} The enzyme is essential for viral replication; consequently, it is an attractive validated target for the development of direct-acting antivirals.^{16–22} SARS-CoV-2 3CL^{pro} has been under intense investigation for the development of SARS-CoV-2 therapeutics by us^{23–29} and others.^{18,30–40} The rationale underlying the targeting of SARS-CoV-2 3CL^{pro} is further buttressed by the first time demonstration of clinical efficacy by a feline coronavirus 3CL^{pro} inhibitor.^{27,28} We report herein the results of preliminary studies related to the structure-guided design of potent inhibitors of SARS-CoV-2 3CL^{pro} (Figure 1/general structure I) that incorporate in their structure a spirocyclic component as a design element to optimally exploit new chemical space in the active site of the protease.

RESULTS AND DISCUSSION

Inhibitor Design Rationale. There is an array of advantages accrued through the judicious use of spirocycles

Received: February 8, 2022

Published: May 31, 2022



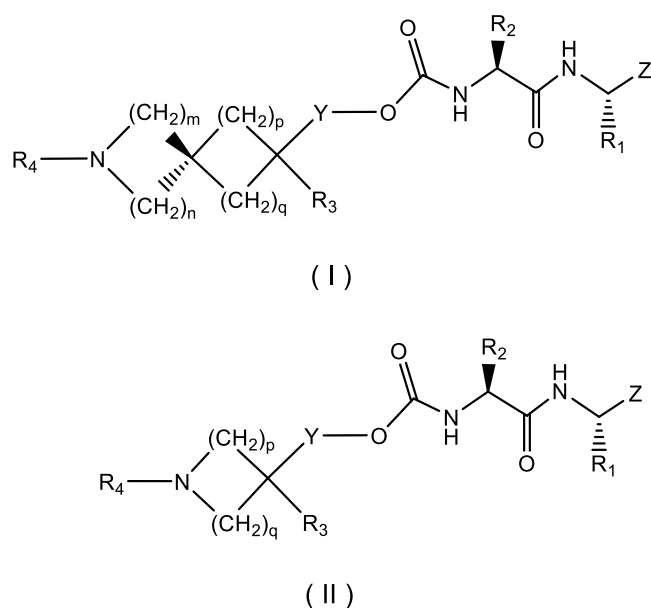


Figure 1. General structures of spirocyclic (I) and azetidine (II) inhibitors.

in drug design, including improved physicochemical and PK characteristics, structural novelty, reduced conformational flexibility, and the capture of favorable binding interactions by probing and exploiting poorly explored regions of chemical space.^{41–43} Importantly, the structural motifs embodied in spirocycles make possible the rigorous control of the spatial disposition of exit vectors; consequently, it was envisaged that the attachment of a suitably decorated spirocycle capable of engaging in favorable binding interactions with the S_4 subsite of SARS-CoV-2 3CL^{pro} to a recognition element that is congruent with the known substrate specificity of the enzyme (a Leu-Gln surrogate fragment) can be leveraged to yield a molecule (Figure 1/general structure I) with high inhibitory prowess. The validity of the approach and the design of the inhibitors was further facilitated by the availability and use of high-resolution cocrystal structures.^{16–18,24–26} Finally, for comparative purposes, a series of azetidine-derived inhibitors (Figure 1/general structure II) were also synthesized and evaluated in biochemical and cell-based assays.

Chemistry. The inhibitors were readily synthesized by attaching a spirocyclic alcohol to a Leu-Gln surrogate fragment incorporating an aldehyde warhead or latent aldehyde bisulfite adduct. The spirocyclic and azetidine-based precursor alcohols were either commercially available or readily synthesized using commercially available ketone or carboxylic acid precursors. The appropriate spirocyclic and azetidine alcohol inputs (Figure 2) were treated with *N,N'*-disuccinimidyl carbonate (DSC),⁴⁴ followed by coupling of the resulting mixed carbonate to amino alcohol **A**. Dess–Martin periodinane oxidation of dipeptidyl alcohol **a** generated the desired aldehydes **b**, which were subsequently transformed into the corresponding aldehyde bisulfite adducts **c** (Scheme 1).⁴⁵

Biochemical Studies. The inhibitory activity of compounds **1–18b/c** toward SARS-CoV-2 3CL^{pro} and MERS-CoV 3CL^{pro} in biochemical assays^{23–25,28} as well as the cytotoxicity of the compounds were determined, and the results are listed in Tables 1 and 2. For comparative purposes, the IC₅₀ and CC₅₀ values of GC376 are included in Table 1.

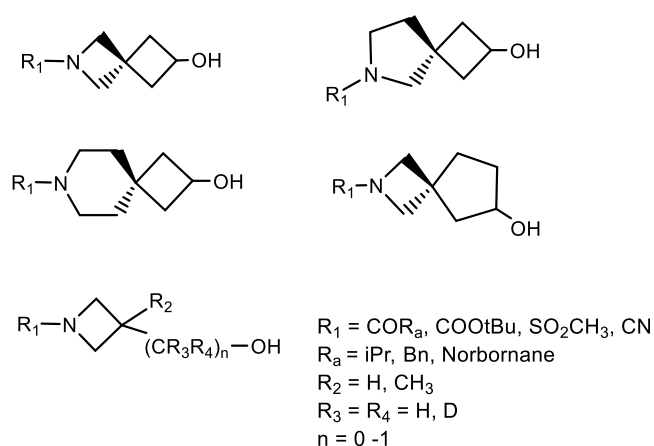


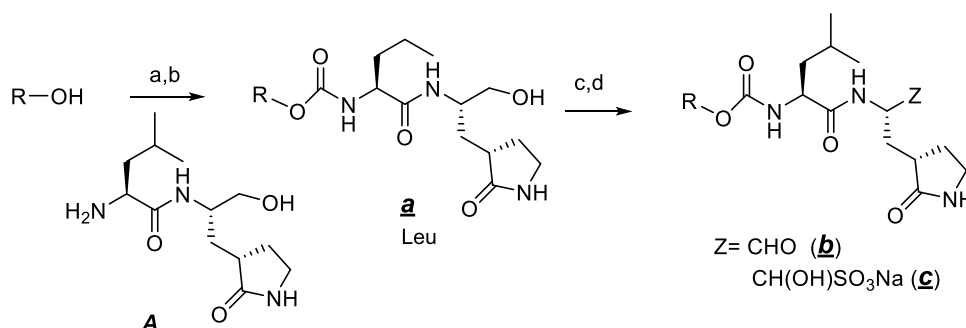
Figure 2. Alcohol precursors to 2-azaspiro [3.3]-, 6-azaspiro [3.5]-, 6-azaspiro [3.4]-, 2-azaspiro [3.4]-, and azetidine-derived inhibitors.

We have previously reported EC₅₀ values determined by the natural infection of SARS-CoV-2 in Vero E6 cells²⁶ as well as a cell-based assay with two plasmids expressing SARS-CoV-2 3CL^{pro} and luciferase fused with the 3CL^{pro} cleavage site (VRLQS) in cells.²⁵ While the latter system is a safe and fast BSL-2-based assay, EC₅₀ values were relatively higher than those by natural infection of SARS-CoV-2 in Vero E6 cells. In this study, we used another BSL2 cell-based replicon assay in 293T cells, mimicking the natural cycle of SARS-CoV-2 replication.⁴⁶ As a control, we used GC376 and the EC₅₀ was calculated at $0.027 \pm 0.01 \mu\text{M}$ in the assay, which is comparable to the value ($0.02 \mu\text{M}$ in 293T cells) previously reported with the same system.⁴⁶ Four compounds were selected for the determination of EC₅₀ values, and inhibition curves by each compound were consistent with a dose-dependent mode and $R^2 > 0.9$ (Figure 3). The selected compounds were potent SARS-CoV-2 inhibitors with EC₅₀ values ranging from 0.08 to $0.43 \mu\text{M}$ (Tables 1 and 2). These were correlated well with IC₅₀ values.

X-ray Crystallographic Studies. To gain insight into and understanding the binding of the spirocyclic inhibitors to the active site of the protease, as well as to identify the structural determinants associated with binding, high-resolution cocrystal structures of SARS-CoV-2 3CL^{pro} and MERS-CoV 3CL^{pro} were obtained in complex with spirocyclic and azetidine-derived inhibitors. For all structures described below, the electron density was consistent with both the R and S enantiomers at the stereocenter formed by covalent attachment of the S_γ atom of Cys 145 or Cys 148 in SARS-CoV-2 3CL^{pro} and MERS-CoV 3CL^{pro}, respectively. Therefore, the alternate conformations were modeled as each enantiomer with 0.5 occupancy.

Azetidine-Derived Inhibitor Bound Structures. In the case of the azetidine inhibitor **14c**, the active site contained a prominent difference electron density consistent with the inhibitor covalently bound to Cys 148 and Cys 145 in each subunit (Figure 4A,B). Inhibitor **14c** forms typical hydrogen bonds to MERS-CoV 3CL^{pro} and SARS-CoV-2 3CL^{pro} (Figure 4C,D) along with an additional contact to the backbone nitrogen atom of Ala 191 in the case of SARS-CoV-2 3CL^{pro}. This places the inhibitor deep within the S_4 subsites, as shown in Figure 5A,B. Superposition of the two structures revealed similar binding modes although the azetidine rings are rotated

Scheme 1. General Synthesis of Inhibitors 1–18b/c



^aDSC/TEA/ACN/RT/4h ^bA/TEA/DCM/RT/3h ^cDMP/DCM/15^oC/3h ^dNaHSO₃/EtOAc/EtOH/50^oC/3h.

in the S₄ subsite approximately 90° relative to one another (Figure S1C).

2-Azaspiro [3.3]-Derived Inhibitor Bound Structures.

Similar to the azetidines inhibitors above, the difference electron density consistent with inhibitors 2c, 3c, and 4c bound in the SARS-CoV-2 3CL^{PRO} active site covalently to Cys 145 (Figure 5A–C). For 2c, the spirocyclic portion of the inhibitor that binds in the S₄ subsite appears to adopt two conformations based on the electron density (Figure 5A). However, the isopropyl groups were disordered in both conformations. Inhibitor 3c also adopted two conformations (Figure 5B), but the benzyl ring at the terminal end was disordered and could not be modeled. Interestingly, 4c appeared to adopt one conformation in the spirocyclic region of the inhibitor (Figure 5C) although electron density for the methylsulfonyl group was not present, which indicated a certain degree of disorder in this region. It may be that the larger isopropyl and benzyl groups in 2c and 3c, respectively, interact transiently with different regions in the S₄ subsite and result in the observed dual conformations in the spirocycle relative to 4c. The inhibitors form the typical hydrogen bonds to the protein (Figure 5D–F) with an additional polar contact observed between the carbonyls of 2c and Leu 167 (Figure 5D). The diverse conformational differences in these inhibitors allow the spirocyclic portion of the compounds to cover a wide region of space within the S₄ subsite, as shown in Figure S2. Overall, the superposition of these structures revealed a high degree of similarity in the ligand conformations. However, as evident in Figure 6, a large degree of motion is present in the spirocyclic region of the compounds with the largest span covering 8.5 Å in the case of inhibitor 2c.

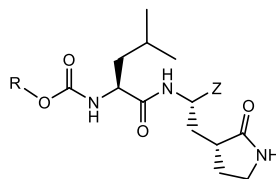
6-Azaspiro [3.5]-Derived Inhibitor Bound Structures.

Interestingly, the spirocyclic inhibitors that contained the larger six-membered nitrogen heterocycle did not display the same degree of disorder observed for 2c, 3c, and 4c, which contain the four-membered rings. This was revealed by the structure determination of 7c, 8c, 9c, 10c, and 11c in complex with SARS-CoV-2 3CL^{PRO}, in which the electron density was well defined for the majority of these inhibitors (Figures 7A–C and S3A,B). These inhibitors form similar hydrogen-bond interactions with the protein that are typically observed that include His 41, His 163, His 164, Glu 166, Gln 189, and bifurcated H-bonds between Glu 166 and Phe 140 and the NH of the δ-lactam ring (Figures 7D–F and S3C,D). However, the structure with 9c adopts an additional polar contact (2.81 Å) between the carbonyl and the backbone carbonyl of Pro 168 (Figure 7E).

Notably, the methylsulfonyl group of 10c is in proximity to Pro 168 but too far to form an interaction (3.4 Å). The interaction between Pro 168 and 9c results in the movement (~2.6 Å) of a nearby loop that includes Leu 167, Pro 168, and Thr 169 relative to the other structures, such as 10c (Figure 8A). Overall, the structures with 7c, 8c, and 11c adopt very similar binding modes (Figure 8B) in which the terminal ends of the inhibitors are positioned between a cleft formed by Glu 166 and Pro 168 (Figure S4A–C). Inhibitor 10c is in an intermediate position as it is closer to Pro 168 within the hydrophobic ridge of the S₄ subsite and 9c is the extreme case in which the benzyl ring is located on top of this ridge (Figure S4D,E). As a whole, these inhibitors occupy a wide range of space within the S₄ subsite spanning approximately 9.5 Å (Figure 8B). Notably, the extended length of the azaspiro[3.5] inhibitors relative to the azaspiro[3.3] compounds permits further engagement with the hydrophobic cleft of the S₄ subsite. Presumably, this “locks” the azaspiro[3.5] inhibitors in a stable conformation and precludes the compounds from adopting multiple conformations (see Figures S2 and S4).

Similarly, the structures of MERS-CoV 3CL^{PRO} with 8c, 9c, and 10c yielded well-defined electron density overall (Figure 9A–C) although the benzyl ring was disordered in 9c. The inhibitors form the typical array of hydrogen-bond interactions with the protein, including Glu 169, His 41, His 166, and bifurcated H-bonds between Glu 169 and Phe 143 and the NH of the δ-lactam ring of the inhibitor (Figure 9D–F). For the structure with 9c, an additional polar contact with the backbone carbonyl of Ala 171 (3.07 Å) positions the molecule in the S₄ subsite in a similar pose to that observed for 8c (Figure S5A,B). Although the carbonyl in the structure of 8c is in a similar orientation to 9c, the distance to the backbone carbonyl of Ala 171 is much larger (4.07 Å). The binding mode of 10c differs from 8c and 9c in that the methylsulfonyl group is positioned deeper within the S₄ subsite (Figure S5C) and is positioned 3.4 Å from His 194 potentially forming a salt-bridge-like interaction. The superimposed structures of MERS-CoV 3CL^{PRO} in complex with 8c, 9c, and 10c (shown in Figure S6) show that these inhibitors span a space within the S₄ subsite of approximately 8.0 Å. Collectively, the structural studies suggest that the use of spirocycles with different exit vectors is well suited to exploiting new chemical space in and around the S₄ subsite.

Structure–Activity Relationships. A representative series of spirocyclic inhibitors derived from 2-azaspiro[3.3]-, 2-azaspiro[3.4]-, 6-azaspiro[3.4]-, and 6-azaspiro[3.5]-spirocycles displaying different exit vectors were synthesized and evaluated in biochemical and cell-based assays. It is evident from the

Table 1. IC₅₀ Values of Spirocyclic Inhibitors 1-11b/c against SARS-CoV-2 3CL^{pro} and MERS-CoV 3CL^{pro}, and CC₅₀ Values

Compound Code	R	Z	IC ₅₀ (μM)		IC ₅₀ (μM) ^a
			SARS-CoV-2 3CL ^{pro}	MERS-CoV 3CL ^{pro}	CC ₅₀ (μM)
1b		-CHO	3.30±0.28	1.50±0.42	>100
1c		-CH(OH)SO ₃ Na	0.85±0.07	0.28±0.11	>100
2b		-CHO	1.15±0.49	0.35±0.07	>100
2c		-CH(OH)SO ₃ Na	0.65±0.07	0.55±0.07	>100
3b		-CHO	0.26±0.04	0.21±0.04	>100
3c		-CH(OH)SO ₃ Na	0.26±0.05	0.13±0.03	>100
4b		-CHO	0.68±0.04	0.22±0.03	>100
4c		-CH(OH)SO ₃ Na	0.76±0.08	0.16±0.01	>100
5b		-CHO	0.45±0.05	0.70±0.14	>100
5c		-CH(OH)SO ₃ Na	0.75±0.07	0.75±0.07	>100
6b		-CHO	1.25±0.07	1.01±0.27	>100
6c		-CH(OH)SO ₃ Na	1.20±0.14	1.30±0.14	>100
7b^b		-CHO	0.36±0.06	1.20±0.14	>100
7c^b		-CH(OH)SO ₃ Na	0.29±0.02	0.95±0.21	>100
8b		-CHO	0.38±0.04	0.65±0.21	>100
8c		-CH(OH)SO ₃ Na	0.41±0.01	0.52±0.12	>100
9b		-CHO	0.35±0.07	0.70±0.14	>100
9c		-CH(OH)SO ₃ Na	0.29±0.06	0.61±0.13	>100
10b		-CHO	0.24±0.01	0.37±0.05	>100
10c		-CH(OH)SO ₃ Na	0.24±0.03	0.33±0.04	>100
11b		-CHO	0.32±0.05	0.56±0.06	>100
11c		-CH(OH)SO ₃ Na	0.39±0.03	0.63±0.18	>100
GC376		-CH(OH)SO ₃ Na	0.41±0.07	0.25±0.10	> 100

^aMean ± SD of at least three replicates. ^bThe EC₅₀ values of the aldehyde and bisulfite salt adduct were determined to be 0.09 ± 0.01 μM and 0.08 ± 0.02 μM, respectively.

results shown in Table 1 that the synthesized compounds generally display high inhibitory activity toward SARS-CoV-2 3CL^{pro} and MERS-CoV 3CL^{pro}, with the IC₅₀ values of most of the inhibitors in the submicromolar range. Furthermore, the compounds are devoid of cytotoxic effects. The IC₅₀ values of spirocycles **7b** and **3b** were found to be >9-fold and nearly 13-fold lower than that of compound **1b**, respectively, suggesting that directional and recognition effects associated with the nature of the spirocycle and R group, respectively, are important in enhancing potency. The importance of exit vectors is also evident in comparing the relative potency of aldehyde inhibitors **1b**, **5b**, and **6b**, which are derived from different spirocycles. The potency of compounds **8b**, **9b**, **10b**,

and **11b** was high and remained invariant to the nature of the R group. Several of the inhibitors were found to be broadly active against both SARS-CoV-2 3CL^{pro} and MERS-CoV 3CL^{pro}, suggesting a high likelihood of identifying a broad-spectrum preclinical candidate. The EC₅₀ values of the aldehyde and the corresponding bisulfite adduct pairs tested were comparable, and one pair was in the nM range (Table 1, compounds **7b/7c**). The safety index (SI), defined as CC₅₀/EC₅₀, for the compounds was very high (~1250). The results shown in Table 1 are congruent with the crystallographic studies (*vide supra*) and validate the use of spirocyclic inhibitors in exploring and exploiting new chemical space in the S₄ region of SARS-CoV-2 3CL^{pro}.

Table 2. IC₅₀ Values of Azetidine Inhibitors 12-18b/c against SARS-CoV-2 3CL^{pro} and MERS-CoV 3CL^{pro}, and CC₅₀ Values

Compound Code	R	Z	IC ₅₀ (μM)		IC ₅₀ (μM) ^a
			SARS-CoV-2 3CL ^{pro}	MERS-CoV 3CL ^{pro}	CC ₅₀ (μM)
12b		-CHO	2.50±0.28	1.65±0.64	>100
12c		-CH(OH)SO ₃ Na	3.05±0.35	2.55±0.92	>100
13b		-CHO	3.65±0.64	3.45±1.20	>100
13c		-CH(OH)SO ₃ Na	2.50±0.57	4.30±0.28	>100
14b ^b		-CHO	0.41±0.04	0.49±0.04	>100
14c ^b		-CH(OH)SO ₃ Na	0.50±0.14	0.44±0.06	>100
15b		-CHO	0.83±0.04	0.28±0.11	>100
15c		-CH(OH)SO ₃ Na	0.76±0.08	0.18±0.01	>100
16b		-CHO	0.52±0.14	0.19±0.04	>100
16c		-CH(OH)SO ₃ Na	0.49±0.02	0.17±0.03	>100
17b		-CHO	4.95±0.49	1.40±0.14	>100
17c		-CH(OH)SO ₃ Na	4.05±0.78	1.35±0.21	>100
18b		-CHO	0.33±0.04	0.35±0.01	>100
18c		-CH(OH)SO ₃ Na	0.34±0.01	0.37±0.06	>100

^aMean ± SD of at least three replicates. ^bThe EC₅₀ values of the aldehyde and bisulfite salt adduct were determined to be 0.38 ± 0.07 (μM) and 0.43 ± 0.16 (μM), respectively.

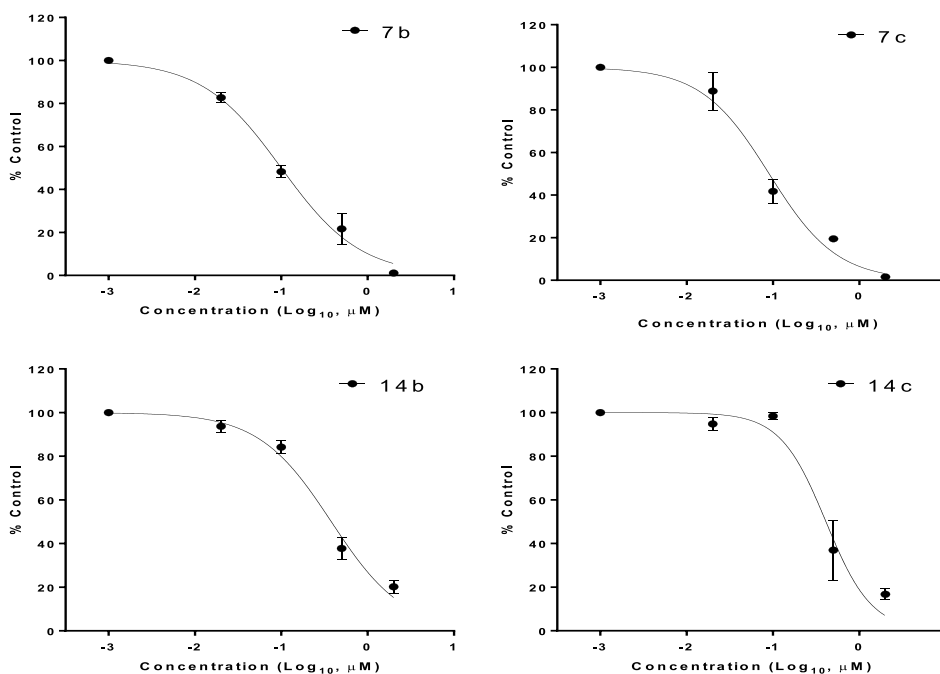


Figure 3. Inhibition curves of selected compounds 7b, 7c, 14b, and 14c in the cell-based SARS-CoV-2 replicon assay.

In the azetidine series, biochemical evaluation of the synthesized azetidine inhibitors revealed that the compounds were fairly potent against both SARS-CoV 3CL^{pro} and MERS-CoV 3CL^{pro} (Table 2). The IC₅₀ values of compounds 14b/14c having an extra methylene group were >6-fold better than those of the 12b/12c pair. Furthermore, in the series of compounds 14b, 15b, 16b, and 17b, potency was found to be sensitive to the nature of the group attached to the azetidine nitrogen, with compound 14b being 12-fold more potent than

17b and with an EC₅₀ value of 0.38 μM. We previously harnessed the benefits accrued through deuteration by demonstrating that deuterated variants of GC376 have enhanced antiviral activity and display efficacy in a fatal mouse model (K18-hACE2 mice) of SARS-CoV-2 infection.²⁶ Thus, the effect of deuteration on pharmacological activity was investigated by determining the IC₅₀ values of a representative deuterated aldehyde and bisulfite adduct pair 18b/18c. These were found to be comparable to those of the corresponding

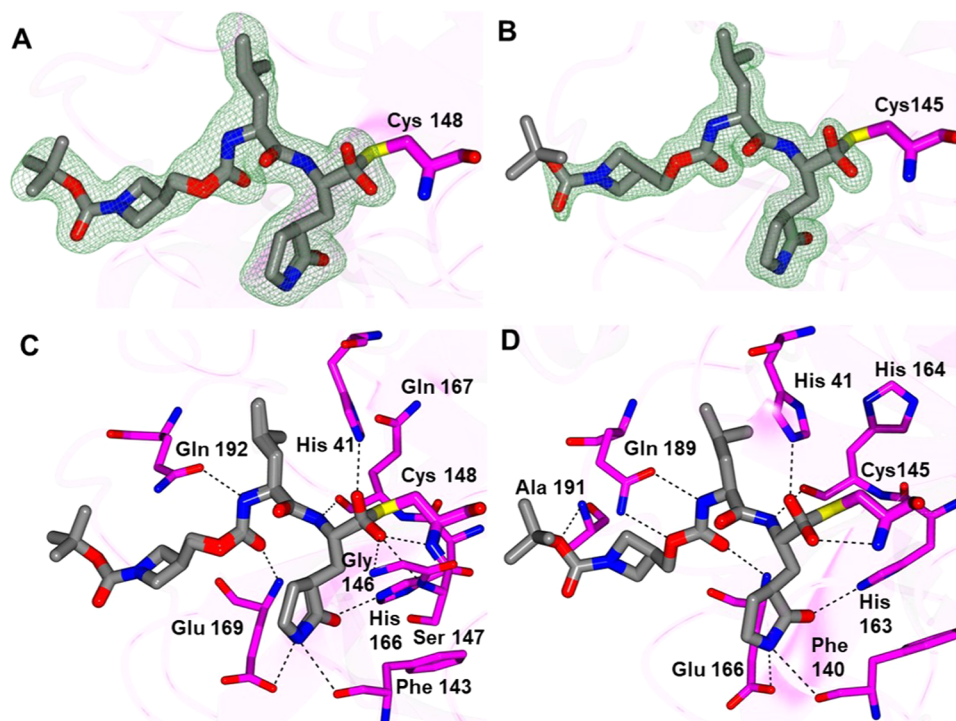


Figure 4. Binding mode of the azetidine-derived inhibitor **14c** to MERS-CoV 3CL^{pro} (A, C) and SARS-CoV-2 3CL^{pro} (B, D). Fo-Fc omit map (green mesh) contoured at 3σ (A, B). Hydrogen-bond interactions (dashed lined) (C, D). PDB IDs: **14c** with MERS-CoV 3CL^{pro} (7T41), **14c** with SARS-CoV-2 3CL^{pro} (7T4B).

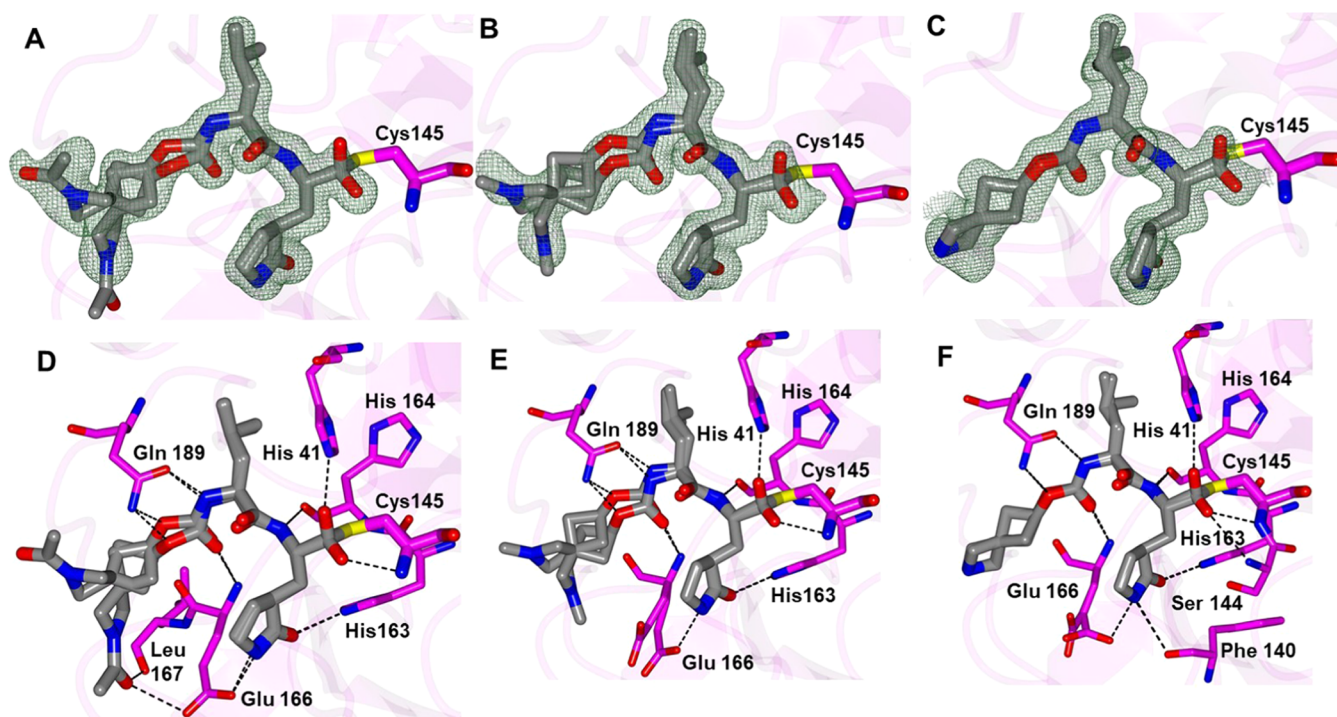


Figure 5. Binding modes of 2-azaspiro [3.3] inhibitors **2c** (A, D), **3c** (B, E), and **4c** (C, F) with SARS-CoV-2 3CL^{pro}. Fo-Fc omit map (green mesh) contoured at 3σ (A–C). Hydrogen-bond interactions (dashed lined) (D–F). PDB IDs: **2c** (7T42), **3c** (7T43), **4c** (7T44).

nondeuterated compounds **14b/14c**. Although not established in the present studies, it is anticipated that deuterated variants of inhibitors reported herein will likely display improved PK characteristics.⁴⁷ These dipeptidyl compounds, including GC376, have inhibitory activity against Cathepin L,⁶² and thus they could act as entry inhibitors against SARS-CoV-2.

When we examined if **7b/7c** and **14b/14c** could inhibit the entry of SARS-CoV-2 using a pseudotyped lentivirus with S,⁶³ the inhibition was moderate with EC₅₀ values in the 2–10 μ M range. Of note, because the EC₅₀'s listed in Tables 1 and 2 were determined with the SARS-CoV-2 replicon system,⁴⁶

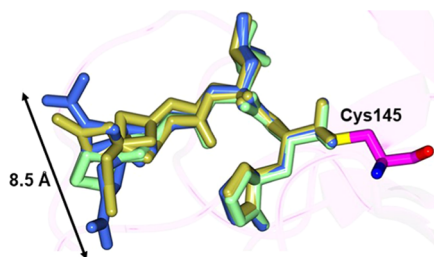


Figure 6. Superposition of **2c** (blue), **3c** (gold), and **4c** (green) inhibitors bound to SARS-CoV-2 3CL^{pro} highlighting the broad conformations in the spirocyclic regions. PDB IDs: **2c** (7T42), **3c** (7T43), **4c** (7T44).

which bypasses entry events, the inhibitory action was likely due to blocking 3CL^{pro}.

CONCLUSIONS

There is currently a need for the development of direct-acting antivirals to complement the use of vaccines and biologics for the treatment of COVID-19. In this study, we have sought to exploit the directional and stereochemical control afforded by spirocycles to optimize potency. The results indicate that the incorporation of spirocyclic elements embellished with appropriate recognition moieties, combined with structural information gained from cocrystal structures, into the design of process has resulted in the identification of highly effective broad-spectrum inhibitors of SARS-CoV-2 3CL^{pro} and MERS-CoV 3CL^{pro}, with EC₅₀ values and safety indices in the 0.08–0.43 μM and 1250–233 range, respectively. The structural determinants associated with binding and the mechanism of action involving the participation of the catalytic dyad Cys145 and His41 and the formation of a tetrahedral adduct were elucidated using X-ray crystallography. These studies provide a solid foundation for conducting further preclinical studies.

EXPERIMENTAL SECTION

General. Reagents and dry solvents were purchased from various chemical suppliers (Advanced ChemBlocks, Sigma-Aldrich, Acros

Organics, Chem-Impex, TCI America, Oakwood chemical, APExBIO, SynQuest, Fisher, and Bachem) and were used as obtained. The synthesized compounds were purified using flash chromatography and silica gel (230–450 mesh) (Sorbent Technologies, Atlanta, GA). Normal-phase chromatography was performed on a Teledyne ISCO CombiFlash system using RediSep normal-phase silica cartridges (35–70 μm particle size range). Thin-layer chromatography was performed using Analtech silica gel plates. Visualization was accomplished using UV light and/or iodine. ¹H NMR spectra were recorded in CDCl₃ or DMSO-*d*₆ using a Varian XL-400 spectrometer. Chemical shifts and coupling constants are reported in parts per million and hertz, respectively. The following abbreviations are used to describe splitting patterns: s, singlet; d, doublet; t, triplet; q, quartet; m, multiplet; br, broad.

The purity of the inhibitors was determined by absolute qNMR analysis using a Bruker AV III 500 NMR spectrometer equipped with a CPDUL CRYOPROBE and CASE autosampler (the University of Kansas Nuclear Magnetic Resonance Laboratory). Dimethyl sulfone TraceCERT was used as the internal calibrant. High-resolution mass spectrometry (HRMS) was performed at the Wichita State University Mass Spectrometry lab using an Orbitrap Velos Pro mass spectrometer (Thermo Fisher, Waltham, MA) equipped with an electrospray ion source. The purity of the compounds in the *b*-series (aldehydes) was found to be ≥90%, and that of the *c*-series (bisulfite adducts) was found to be ≥95%. Note: the generated aldehydes are prone to facile racemization involving the α-carbon of the aldehyde group. The protocol used to minimize racemization included fast and rigorous workup (<1 h) and rapid flash chromatography (silica gel/ethyl acetate/hexane gradient; <1 h). This protocol invariably yields aldehydes with racemization in the 0–5% range. With certain aldehydes, attainment of low racemization resulted in lower than 95% purity due to incomplete removal of Dess-Periodinane byproducts.

Synthesis of Compounds. *Preparation of Compounds 1–18a.* **General Procedure.** To a solution of alcohol (1 equiv) (Table 1) in anhydrous acetonitrile (10 mL/g alcohol) were added *N,N'*-disuccinimidyl carbonate (1.2 equiv) and TEA (3.0 equiv), and the reaction mixture was stirred for 4 h at room temperature. The solvent was removed *in vacuo*, and the residue was dissolved in ethyl acetate (40 mL/g alcohol). The organic phase was washed with saturated aqueous NaHCO₃ (2 × 20 mL/g alcohol), followed by brine (20 mL/g alcohol). The organic layers were combined and dried over anhydrous Na₂SO₄, filtered, and concentrated *in vacuo* to yield the

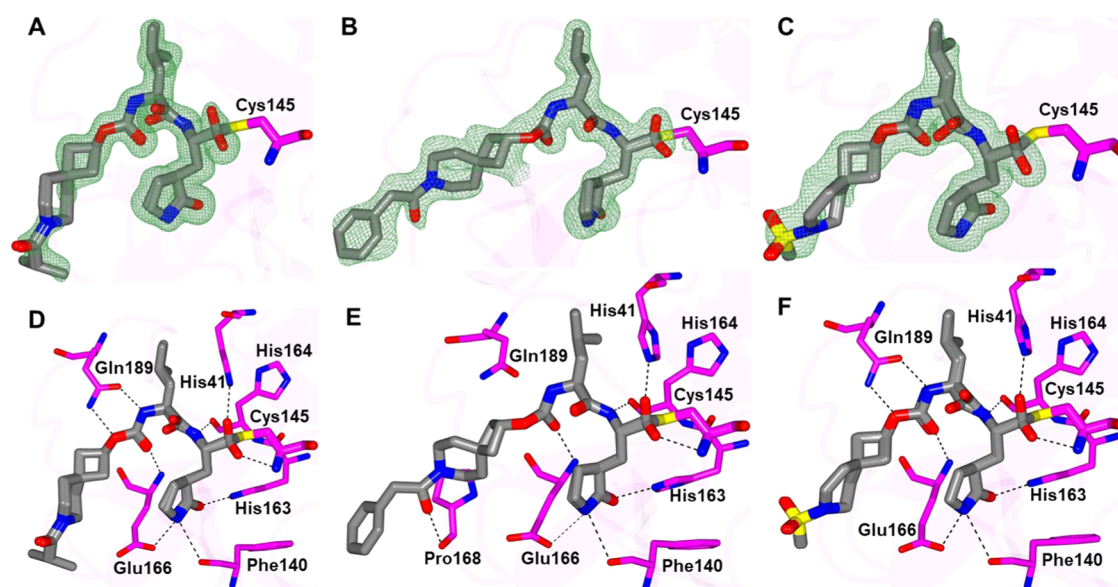


Figure 7. Binding modes of 6-azaspiro [3.5] inhibitors **8c** (A, D), **9c** (B, E), and **10c** (C, F) with SARS-CoV-2 3CL^{pro}. Fo-Fc omit map (green mesh) contoured at 3σ (A–C). Hydrogen-bond interactions (dashed lined) (D–F). PDB IDs: **8c** (7T46), **9c** (7T48), **10c** (7T49).

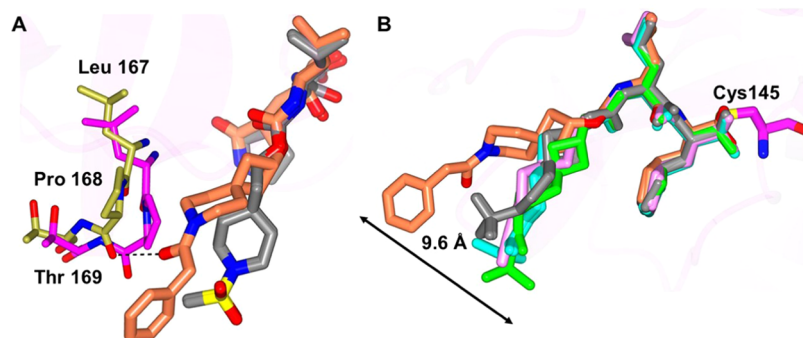


Figure 8. Comparison of 6-azaspiro [3.5] inhibitors complexed with SARS-CoV-2 3CL^{Pro}. Superposition of 9c (coral) and 10c (gray) in complex with SARS-CoV-2 3CL^{Pro}. The protein residues are colored gold and magenta for 9c and 10c, respectively (A). Superposition of 7c (green), 8c (cyan), 9c (coral), 10c (gray), and 11c (pink) (B). PDB IDs: 7c (7T45), 8c (7T46), 9c (7T48), 10c (7T49), 11c (7T4A).

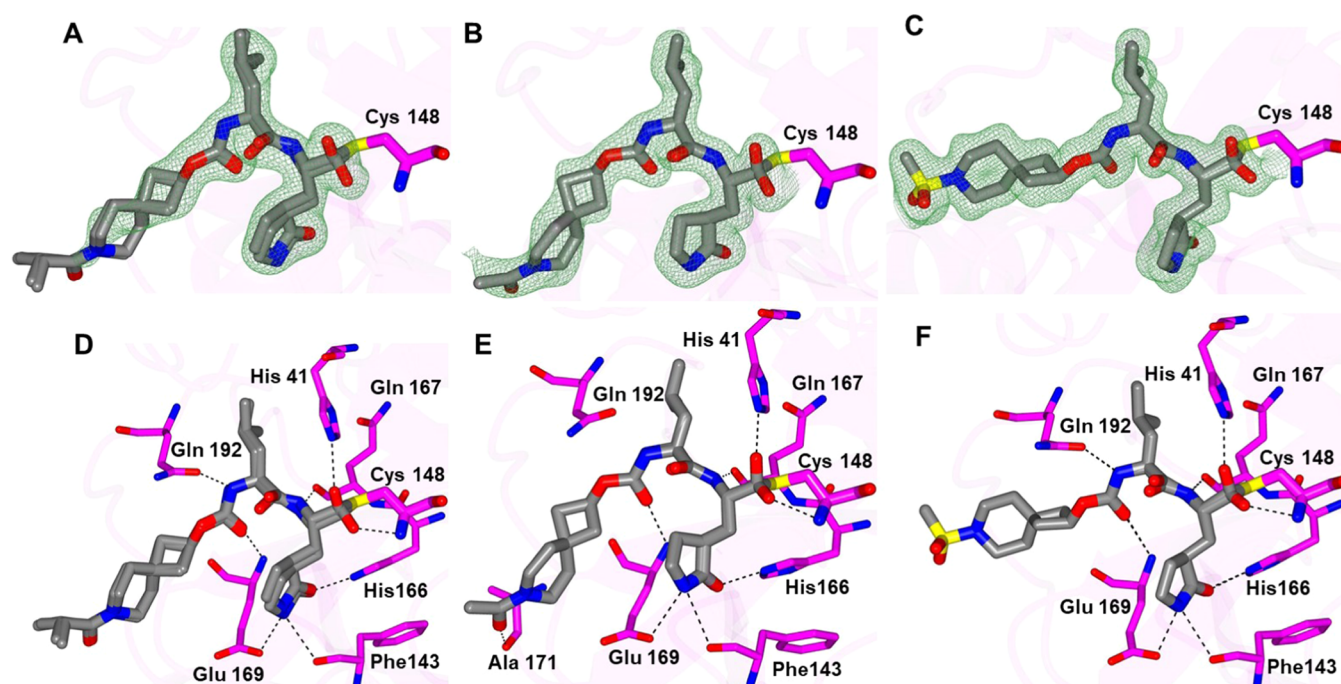


Figure 9. Binding modes of 6-azaspiro [3.5] inhibitors 8c (A, D), 9c (B, E), and 10c (C, F) with MERS-CoV 3CL^{Pro}. Fo-Fc omit map (green mesh) contoured at 3σ (A–C). Hydrogen-bond interactions (dashed lined) (D–F). PDB IDs: 8c (7T3Y), 9c (7T3Z), 10c (7T4O).

mixed carbonate, which was used in the next step without further purification.

To a solution of Leu-Gln surrogate amino alcohol A (1.0 equiv) in dry methylene chloride (10 mL/g of amino alcohol) was added TEA (1.5 equiv), and the reaction mixture was stirred for 20 min at room temperature (solution 1). In a separate flask, the mixed carbonate was dissolved in dry methylene chloride (10 mL/g of carbonate) (solution 2). Solution 1 was added to solution 2, and the reaction mixture was stirred for 3 h at room temperature. Methylene chloride was added to the organic phase (40 mL/g of carbonate) and then washed with saturated aqueous NaHCO₃ (2 × 20 mL/g alcohol), followed by brine (20 mL/g alcohol). The organic phase was dried over anhydrous Na₂SO₄, filtered, and concentrated *in vacuo*. The resultant crude product was purified by flash chromatography (hexane/ethyl acetate) to yield dipeptidyl alcohol a as a white solid.

Preparation of Compounds 1–18b. General Procedure. To a solution of dipeptidyl alcohol a (1 equiv) in anhydrous dichloromethane (100 mL/g dipeptidyl alcohol) kept at 0–5 °C under a N₂ atmosphere was added Dess–Martin periodinane reagent (3.0 equiv), and the reaction mixture was stirred for 3 h at 15–20 °C. The organic phase was washed with 10% aq Na₂S₂O₃ (2 × 100 mL/g dipeptidyl alcohol), followed by saturated aqueous NaHCO₃ (2 × 100 mL/g

dipeptidyl alcohol), distilled water (2 × 100 mL/g dipeptidyl alcohol), and brine (100 mL/g dipeptidyl alcohol). The organic phase was dried over anhydrous Na₂SO₄, filtered, and concentrated *in vacuo*. The resulting crude product was purified by flash chromatography (hexane/ethyl acetate) to yield aldehyde b as a white solid.

tert-Butyl 6-(((*S*)-4-methyl-1-oxo-1-(((*S*)-1-oxo-3-((*R*)-2-oxopyrrolidin-3-yl)propan-2-yl)amino)pentan-2-yl)carbamoyloxy)-2-azaspiro[3.3]heptane-2-carboxylate (**1b**). ¹H NMR (500 MHz, DMSO-*d*₆) δ 9.38 (d, *J* = 6.9 Hz, 1H), 8.44 (d, *J* = 7.6 Hz, 1H), 7.53 (s, 1H), 7.33 (d, *J* = 8.1 Hz, 1H), 4.74–4.60 (m, 1H), 4.08–3.89 (m, 2H), 3.81 (d, *J* = 26.2 Hz, 4H), 3.19–3.04 (m, 2H), 2.30–2.02 (m, 7H), 1.98–1.74 (m, 2H), 1.71–1.38 (m, 3H), 1.36 (s, 9H), 0.86 (ddd, *J* = 14.0, 10.5, 6.4 Hz, 6H). Yield (74%). HRMS *m/z*: [M + Na]⁺ calc for C₂₅H₄₀N₄NaO₇, 531.2795; found, 531.2776.

2-Isobutyryl-2-azaspiro[3.3]heptan-6-yl ((*S*)-4-methyl-1-oxo-1-(((*S*)-1-oxo-3-((*R*)-2-oxopyrrolidin-3-yl)propan-2-yl)amino)pentan-2-yl)carbamate (**2b**). Yield (24%). ¹H NMR (400 MHz, cdCl₃) δ 9.58 (s, 1H), 6.69 (s, 1H), 5.88 (s, 1H), 5.68 (s, 1H), 5.23–4.79 (m, 2H), 4.38–4.09 (m, 2H), 4.02–3.89 (m, 2H), 3.78–3.66 (m, 2H), 3.63–3.54 (m, 2H), 3.51–3.24 (m, 4H), 2.69–2.19 (m, 2H), 2.19–1.98 (m, 1H), 1.98–1.37 (m, 5H), 1.19–1.10 (m, 6H), 1.03–0.79 (m,

6H). HRMS m/z : $[M + Na]^+$ calc for $C_{24}H_{38}N_4NaO_6$ 501.2689; found, 501.2672.

2-(2-Phenylacetyl)-2-azaspiro[3.3]heptan-6-yl ((S)-4-methyl-1-oxo-1-(((S)-1-oxo-3-((R)-2-oxopyrrolidin-3-yl)propan-2-yl)amino)pentan-2-yl)carbamate (3b). Yield (69%). 1H NMR (400 MHz, $cdCl_3$) δ 9.46 (s, 1H), 8.95 (d, $J = 5.1$ Hz, 1H), 7.40–7.22 (m, 5H), 6.61 (s, 1H), 5.87 (s, 1H), 5.17 (d, $J = 8.5$ Hz, 1H), 4.94–4.86 (m, 1H), 4.35–4.25 (m, 1H), 4.25–4.17 (m, 1H), 3.63–3.53 (m, 2H), 3.53–3.39 (m, 4H), 3.37–3.29 (m, 2H), 2.51–2.35 (m, 2H), 2.33–2.10 (m, 2H), 2.09–1.96 (m, 1H), 1.94–1.62 (m, 5H), 1.57–1.44 (m, 1H), 1.01–0.89 (m, 6H). HRMS m/z : $[M + Na]^+$ calc for $C_{28}H_{38}N_4NaO_6$ 549.2689; found, 549.2675.

2-(Methylsulfonyl)-2-azaspiro[3.3]heptan-6-yl ((S)-4-methyl-1-oxo-1-(((S)-1-oxo-3-((R)-2-oxopyrrolidin-3-yl)propan-2-yl)amino)pentan-2-yl)carbamate (4b). Yield (16%). 1H NMR (400 MHz, $cdCl_3$) δ 9.45 (s, 1H), 8.12 (s, 1H), 6.67 (s, 1H), 6.24 (s, 1H), 5.03–4.79 (m, 1H), 4.23 (t, $J = 11.4$ Hz, 1H), 4.00–3.87 (m, 1H), 3.71–3.54 (m, 4H), 3.44–3.16 (m, 6H), 2.99 (s, 3H), 2.52–2.28 (m, 2H), 2.26–1.71 (m, 3H), 1.68–1.45 (m, 3H), 1.05–0.78 (m, 6H). HRMS m/z : $[M + Na]^+$ calc for $C_{21}H_{34}N_4NaO_7S$ 509.2046; found, 509.1988.

tert-Butyl 2-(((S)-4-methyl-1-oxo-1-(((S)-1-oxo-3-((R)-2-oxopyrrolidin-3-yl)propan-2-yl)amino)pentan-2-yl)carbamoyloxy)-6-azaspiro[3.4]octane-6-carboxylate (5b). Yield (88%). 1H NMR (400 MHz, $cdCl_3$) δ 9.49 (s, 1H), 8.34 (s, 1H), 6.06 (s, 1H), 5.28–5.17 (m, 1H), 5.02–4.89 (m, 1H), 4.38–4.12 (m, 2H), 3.47–3.19 (m, 6H), 2.55–2.29 (m, 4H), 2.19–1.80 (m, 7H), 1.80–1.61 (m, 2H), 1.61–1.49 (m, 1H), 1.45 (s, 9H), 1.01–0.89 (m, 6H). HRMS m/z : $[M + Na]^+$ calc for $C_{26}H_{42}N_4NaO_7S$ 545.2951; found, 545.2931.

tert-Butyl 6-(((S)-4-methyl-1-oxo-1-(((S)-1-oxo-3-((R)-2-oxopyrrolidin-3-yl)propan-2-yl)amino)pentan-2-yl)carbamoyloxy)-2-azaspiro[3.4]octane-2-carboxylate (6b). Yield (67%). 1H NMR (400 MHz, $DMSO-d_6$) δ 9.40 (d, $J = 2.0$ Hz, 1H), 7.71–7.44 (m, 2H), 7.16 (dt, $J = 51.0, 7.3$ Hz, 1H), 5.01–4.83 (m, 1H), 4.65 (t, $J = 5.6$ Hz, 1H), 4.19 (td, $J = 7.7, 4.0$ Hz, 1H), 4.07–3.84 (m, 1H), 3.87–3.49 (m, 5H), 3.39–3.03 (m, 3H), 2.75–2.70 (m, 1H), 2.32–1.94 (m, 3H), 1.94–1.69 (m, 4H), 1.69–1.57 (m, 3H), 1.37 (s, 9H), 0.95–0.81 (m, 6H). HRMS m/z : $[M + Na]^+$ calc for $C_{26}H_{42}N_4NaO_7S$ 545.2951; found, 545.2928.

tert-Butyl 2-(((S)-4-methyl-1-oxo-1-(((S)-1-oxo-3-((R)-2-oxopyrrolidin-3-yl)propan-2-yl)amino)pentan-2-yl)carbamoyloxy)-7-azaspiro[3.5]nonane-7-carboxylate (7b). Yield (67%). 1H NMR (500 MHz, $DMSO-d_6$) δ 7.63 (s, 1H), 7.51 (d, $J = 6.9$ Hz, 1H), 7.22–7.16 (m, 1H), 4.86–4.78 (m, 1H), 4.07–3.91 (m, 2H), 3.28–3.03 (m, 6H), 2.30–2.02 (m, 4H), 1.89–1.77 (m, 2H), 1.75–1.50 (m, 4H), 1.49–1.40 (m, 7H), 1.40 (s, 9H), 0.93–0.80 (m, 6H). HRMS m/z : $[M + H]^+$ calc for $C_{27}H_{45}N_4O_7$ 537.3288; found, 537.3257.

7-Isobutyl-7-azaspiro[3.5]nonan-2-yl ((S)-4-methyl-1-oxo-1-(((S)-1-oxo-3-((R)-2-oxopyrrolidin-3-yl)propan-2-yl)amino)pentan-2-yl)carbamate (8b). Yield (55%). 1H NMR (400 MHz, $cdCl_3$) δ 9.49 (s, 1H), 8.33 (s, 1H), 6.21–6.13 (m, 1H), 5.29–5.22 (m, 1H), 5.01–4.93 (m, 1H), 4.32 (s, 2H), 3.61–3.45 (m, 2H), 3.44–3.28 (m, 4H), 2.82–2.69 (m, 1H), 2.54–2.27 (m, 5H), 2.12–1.93 (m, 2H), 1.92–1.81 (m, 3H), 1.79–1.63 (m, 1H), 1.56 (s, 5H), 1.10 (d, $J = 6.7$ Hz, 6H), 0.97 (d, $J = 6.2$ Hz, 6H). HRMS m/z : $[M + Na]^+$ calc for $C_{26}H_{42}N_4NaO_6$ 529.3002; found, 529.2985.

7-(2-Phenylacetyl)-7-azaspiro[3.5]nonan-2-yl ((S)-4-methyl-1-oxo-1-(((S)-1-oxo-3-((R)-2-oxopyrrolidin-3-yl)propan-2-yl)amino)pentan-2-yl)carbamate (9b). Yield (87%). 1H NMR (400 MHz, $cdCl_3$) δ 9.48 (s, 1H), 8.32 (s, 1H), 7.35–7.15 (m, 5H), 6.19 (d, $J = 13.8$ Hz, 1H), 5.28–5.21 (m, 1H), 5.00–4.86 (m, 1H), 4.37–4.10 (m, 2H), 3.72 (s, 2H), 3.59–3.44 (m, 2H), 3.42–3.23 (m, 4H), 2.52–2.34 (m, 2H), 2.34–2.18 (m, 2H), 2.12–1.90 (m, 1H), 1.90–1.76 (m, 3H), 1.74–1.60 (m, 1H), 1.58–1.43 (m, 4H), 1.41–1.32 (m, 3H), 0.96 (d, $J = 6.1$ Hz, 6H). HRMS m/z : $[M + H]^+$ calc for $C_{30}H_{43}N_4O_6$ 555.3182; found, 555.3156.

7-(Methylsulfonyl)-7-azaspiro[3.5]nonan-2-yl ((S)-4-methyl-1-oxo-1-(((S)-1-oxo-3-((R)-2-oxopyrrolidin-3-yl)propan-2-yl)amino)pentan-2-yl)carbamate (10b). Yield (62%). 1H NMR (400 MHz, $cdCl_3$) δ 9.49 (s, 1H), 8.33 (d, $J = 5.8$ Hz, 1H), 6.10 (s, 1H), 5.25 (d, $J = 8.6$ Hz, 1H), 5.03–4.89 (m, 1H), 4.31 (s, 2H), 3.44–3.29 (m, 2H),

3.21–3.00 (m, 4H), 2.76 (s, 3H), 2.55–2.20 (m, 4H), 2.09–1.80 (m, 4H), 1.69 (td, $J = 12.3, 7.5$ Hz, 7H), 1.54 (t, $J = 8.8$ Hz, 1H), 0.97 (d, $J = 6.2$ Hz, 6H). HRMS m/z : $[M + Na]^+$ calc for $C_{23}H_{38}N_4NaO_7S$ 537.2359; found, 537.2341.

7-Cyano-7-azaspiro[3.5]nonan-2-yl ((S)-4-methyl-1-oxo-1-(((S)-1-oxo-3-((R)-2-oxopyrrolidin-3-yl)propan-2-yl)amino)pentan-2-yl)carbamate (11b). Yield (53%). 1H NMR (400 MHz, $cdCl_3$) δ 9.49 (s, 1H), 8.36 (d, $J = 5.7$ Hz, 1H), 5.95 (s, 1H), 5.21 (d, $J = 8.3$ Hz, 1H), 5.04–4.89 (m, 1H), 4.38–4.25 (m, 2H), 3.45–3.30 (m, 2H), 3.19–3.08 (m, 4H), 2.56–2.22 (m, 4H), 2.01–1.81 (m, 4H), 1.77–1.62 (m, 7H), 1.61–1.48 (m, 1H), 0.97 (d, $J = 5.8$ Hz, 6H). HRMS m/z : $[M + Na]^+$ calc for $C_{23}H_{35}N_5NaO_5$ 484.2536; found, 484.2522.

tert-Butyl 3-(((S)-4-methyl-1-oxo-1-(((S)-1-oxo-3-((R)-2-oxopyrrolidin-3-yl)propan-2-yl)amino)pentan-2-yl)carbamoyloxy)-azetidine-1-carboxylate (12b). Yield (74%). 1H NMR (500 MHz, $DMSO-d_6$) δ 7.78 (s, 1H), 7.68–7.61 (m, 1H), 7.54–7.47 (m, 1H), 5.01–4.90 (m, 1H), 4.19–4.05 (m, 2H), 4.05–3.61 (m, 4H), 3.26–3.04 (m, 2H), 2.27–2.02 (m, 3H), 1.86–1.71 (m, 2H), 1.70–1.39 (m, 4H), 1.38–1.34 (m, 9H), 0.92–0.79 (m, 6H). HRMS m/z : $[M + Na]^+$ calc for $C_{22}H_{36}N_4NaO_7$ 491.2482; found, 491.2461.

tert-Butyl 3-methyl-3-(((S)-4-methyl-1-oxo-1-(((S)-1-oxo-3-((R)-2-oxopyrrolidin-3-yl)propan-2-yl)amino)pentan-2-yl)carbamoyloxy)-azetidine-1-carboxylate (13b). Yield (76%). 1H NMR (400 MHz, $DMSO-d_6$) δ 9.40 (d, $J = 4.9$ Hz, 1H), 8.45 (d, $J = 7.8$ Hz, 1H), 7.63 (s, 1H), 7.50 (d, $J = 7.7$ Hz, 1H), 4.22 (ddd, $J = 11.6, 7.7, 3.9$ Hz, 1H), 4.08–3.93 (m, 1H), 3.88 (d, $J = 9.3$ Hz, 2H), 3.78 (d, $J = 9.4$ Hz, 2H), 3.23–3.02 (m, 2H), 2.34–2.07 (m, 2H), 1.96–1.84 (m, 1H), 1.63 (ddt, $J = 16.1, 11.8, 6.3$ Hz, 3H), 1.55 (s, 3H), 1.46 (qd, $J = 8.4, 3.9$ Hz, 2H), 1.37 (s, 9H), 0.93–0.82 (m, 6H). HRMS m/z : $[M + Na]^+$ calc for $C_{23}H_{38}N_4NaO_7S$ 505.2638; found, 505.2621.

tert-Butyl 3-(((S)-4-methyl-1-oxo-1-(((S)-1-oxo-3-((R)-2-oxopyrrolidin-3-yl)propan-2-yl)amino)pentan-2-yl)carbamoyloxy)-methylazetidine-1-carboxylate (14b). Yield (90%). 1H NMR (400 MHz, $DMSO-d_6$) δ 9.40 (s, 1H), 8.45 (d, $J = 7.5$ Hz, 1H), 7.63 (s, 1H), 7.40 (d, $J = 7.9$ Hz, 1H), 4.21–3.99 (m, 3H), 3.92–3.82 (m, 2H), 3.62–3.52 (m, 2H), 3.21–3.05 (m, 2H), 2.83–2.72 (m, 2H), 2.34–2.06 (m, 2H), 1.95–1.83 (m, 2H), 1.70–1.56 (m, 3H), 1.52–1.42 (m, 1H), 1.37 (s, 9H), 0.92–0.83 (m, 6H). HRMS m/z : $[M + Na]^+$ calc for $C_{23}H_{38}N_4NaO_7S$ 505.2638; found, 505.2609.

(1-(2-Phenylacetyl)azetidin-3-yl)methyl ((S)-4-methyl-1-oxo-1-(((S)-1-oxo-3-((R)-2-oxopyrrolidin-3-yl)propan-2-yl)amino)pentan-2-yl)carbamate (15b). Yield (63%). 1H NMR (400 MHz, $cdCl_3$) δ 9.46 (s, 1H), 8.73–8.66 (m, 1H), 7.40–7.16 (m, 5H), 6.38 (d, $J = 32.7$ Hz, 1H), 6.14 (d, $J = 22.3$ Hz, 1H), 5.32 (d, $J = 16.0$ Hz, 1H), 4.35–3.89 (m, 4H), 3.81–3.65 (m, 2H), 3.60–3.43 (m, 2H), 3.40–3.13 (m, 4H), 2.57–2.19 (m, 2H), 2.06 (s, 1H), 1.98–1.77 (m, 2H), 1.75–1.61 (m, 2H), 1.57–1.45 (m, 1H), 1.03–0.82 (m, 6H). HRMS m/z : $[M + Na]^+$ calc for $C_{26}H_{36}N_4NaO_6$ 523.2533; found, 523.2518.

(1-(Bicyclo[2.2.1]heptane-2-carbonyl)azetidin-3-yl)methyl ((S)-4-methyl-1-oxo-1-(((S)-1-oxo-3-((R)-2-oxopyrrolidin-3-yl)propan-2-yl)amino)pentan-2-yl)carbamate (16b). Yield (75%). 1H NMR (400 MHz, $cdCl_3$) δ 9.47 (s, 1H), 8.85 (s, 1H), 6.28 (d, $J = 42.6$ Hz, 1H), 6.10 (d, $J = 32.7$ Hz, 1H), 5.32–5.28 (m, 1H), 4.45–3.98 (m, 5H), 3.94–3.70 (m, 1H), 3.69–3.52 (m, 2H), 3.51–3.16 (m, 3H), 2.69–2.56 (m, 1H), 2.56–2.21 (m, 5H), 1.96–1.67 (m, 6H), 1.66–1.46 (m, 2H), 1.43–1.23 (m, 3H), 1.18 (q, $J = 8.3$ Hz, 1H), 0.97 (d, $J = 5.6$ Hz, 6H). HRMS m/z : $[M + Na]^+$ calc for $C_{26}H_{40}N_4NaO_6$ 527.2846; found, 527.2837.

(1-(Methylsulfonyl)azetidin-3-yl)methyl ((S)-4-methyl-1-oxo-1-(((S)-1-oxo-3-((R)-2-oxopyrrolidin-3-yl)propan-2-yl)amino)pentan-2-yl)carbamate (17b). Yield (14%). 1H NMR (400 MHz, $cdCl_3$) δ 9.48 (s, 1H), 8.28 (d, $J = 7.5$ Hz, 1H), 6.56 (s, 1H), 5.54 (s, 1H), 4.46–3.91 (m, 2H), 3.90–3.73 (m, 2H), 3.70–3.10 (m, 4H), 3.02–2.71 (m, 2H), 2.57–2.16 (m, 3H), 2.16–1.78 (m, 1H), 1.75–1.48 (m, 3H), 1.46–1.36 (m, 2H), 1.26 (s, 3H), 1.08–0.78 (m, 6H). HRMS m/z : $[M + Na]^+$ calc for $C_{19}H_{32}N_4NaO_7S$ 483.1890; found, 483.1832.

tert-Butyl 3-(((S)-4-methyl-1-oxo-1-(((S)-1-oxo-3-((R)-2-oxopyrrolidin-3-yl)propan-2-yl)amino)pentan-2-yl)carbamoyloxy)-methyl-d2azetidine-1-carboxylate (18b). Yield (80%). 1H NMR (400 MHz, $dmsO$) δ 9.40 (s, 1H), 8.45 (d, $J = 7.6$ Hz, 1H), 7.64 (s,

1H), 7.40 (d, $J = 7.9$ Hz, 1H), 4.23–4.13 (m, 1H), 4.11–3.98 (m, 1H), 3.94–3.79 (m, 2H), 3.63–3.52 (m, 2H), 3.21–3.05 (m, 2H), 2.77 (d, $J = 5.6$ Hz, 1H), 2.38–2.07 (m, 2H), 1.95–1.83 (m, 1H), 1.72–1.58 (m, 3H), 1.52–1.39 (m, 2H), 1.36 (s, 9H), 0.87 (dd, $J = 10.2, 6.6$ Hz, 6H). HRMS m/z : $[M + Na]^+$ calc for $C_{23}H_{36}D_2N_4NaO_7$ 507.2764; found, 507.2768.

Preparation of Compounds 1–18c. General Procedure. To a solution of dipeptidyl aldehyde **b** (1 equiv) in ethyl acetate (10 mL/g of dipeptidyl aldehyde) was added absolute ethanol (5 mL/g of dipeptidyl aldehyde) with stirring, followed by a solution of sodium bisulfite (1 equiv) in water (1 mL/g of dipeptidyl aldehyde). The reaction mixture was stirred for 3 h at 50 °C. The reaction mixture was allowed to cool to room temperature and then vacuum-filtered. The solid was thoroughly washed with absolute ethanol, and the filtrate was dried over anhydrous sodium sulfate, filtered, and concentrated to yield a white solid. The white solid was stirred with dry ethyl ether (3 × 10 mL/g of dipeptidyl aldehyde), followed by careful removal of the solvent using a pipette, and dried using a vacuum pump for 2 h to yield dipeptidyl bisulfite adduct **c** as a white solid.

Sodium (2S)-2-((S)-2-(((2-tert-butoxycarbonyl)-2-azaspiro[3.3]heptan-6-yl)oxy)carbonyl)amino)-4-methylpentanamido)-1-hydroxy-3-((R)-2-oxopyrrolidin-3-yl)propane-1-sulfonate (1c). Yield (56%). ¹H NMR (400 MHz, DMSO- d_6) δ 7.52 (d, $J = 9.3$ Hz, 1H), 7.44 (s, 1H), 7.18 (d, $J = 8.2$ Hz, 1H), 5.71 (d, $J = 5.9$ Hz, 1H), 4.74–4.59 (m, 2H), 4.08–3.58 (m, 5H), 3.23–2.99 (m, 2H), 2.29–1.94 (m, 4H), 1.91–1.71 (m, 1H), 1.69–1.38 (m, 7H), 1.35 (s, 9H), 0.91–0.79 (m, 6H). HRMS m/z : $[M + Na]^+$ calc for $C_{25}H_{41}N_4Na_2O_{10}S$ 635.2339; found, 635.2379.

Sodium (2S)-1-hydroxy-2-((S)-2-(((2-isobutyryl)-2-azaspiro[3.3]heptan-6-yl)oxy)carbonyl)amino)-4-methylpentanamido)-3-((R)-2-oxopyrrolidin-3-yl)propane-1-sulfonate (2c). Yield (69%). ¹H NMR (400 MHz, DMSO- d_6) δ 7.85 (s, 1H), 7.64 (s, 1H), 7.19 (s, 1H), 5.80–5.66 (m, 1H), 4.90–4.60 (m, 2H), 4.28–3.81 (m, 2H), 3.81–3.59 (m, 2H), 3.25–2.98 (m, 4H), 2.47–2.34 (m, 1H), 2.34–1.75 (m, 7H), 1.75–1.29 (m, 4H), 1.01 (d, $J = 6.8$ Hz, 6H), 0.95–0.77 (m, 6H). HRMS m/z : $[M + H]^+$ calc for $C_{24}H_{40}N_4NaO_9S$ 583.2413; found, 583.2675.

Sodium (2S)-1-hydroxy-2-((S)-4-methyl-2-(((2-phenylacetyl)-2-azaspiro[3.3]heptan-6-yl)oxy)carbonyl)amino)pentanamido)-3-((R)-2-oxopyrrolidin-3-yl)propane-1-sulfonate (3c). Yield (97%). ¹H NMR (400 MHz, DMSO- d_6) δ 8.41–8.32 (m, 1H), 8.21 (dd, $J = 13.7, 7.3$ Hz, 1H), 7.47 (d, $J = 3.9$ Hz, 1H), 7.35–7.14 (m, 5H), 5.55 (dd, $J = 188.2, 6.3$ Hz, 1H), 4.86–4.70 (m, 1H), 4.07–3.87 (m, 2H), 3.86–3.54 (m, 2H), 3.49–3.42 (m, 2H), 3.42–3.31 (m, 4H), 3.29–2.99 (m, 2H), 2.32–1.85 (m, 6H), 1.70–1.49 (m, 2H), 1.49–1.39 (m, 2H), 0.93–0.79 (m, 6H). HRMS m/z : $[M + H]^+$ calc for $C_{28}H_{40}N_4NaO_9S$ 631.2853; found, 631.2413.

Sodium (2S)-1-hydroxy-2-((S)-4-methyl-2-(((2-(methylsulfonyl)-2-azaspiro[3.3]heptan-6-yl)oxy)carbonyl)amino)pentanamido)-3-((R)-2-oxopyrrolidin-3-yl)propane-1-sulfonate (4c). Yield (90%). ¹H NMR (400 MHz, DMSO- d_6) δ 7.63 (s, 1H), 7.37 (d, $J = 8.0$ Hz, 1H), 7.19–7.15 (m, 1H), 5.73–5.67 (m, 1H), 5.01–4.78 (m, 2H), 4.78–4.59 (m, 1H), 4.09–3.67 (m, 6H), 3.23–2.98 (m, 4H), 2.91 (s, 3H), 2.38–2.06 (m, 4H), 2.06–1.76 (m, 2H), 1.73–1.53 (m, 1H), 1.53–1.33 (m, 1H), 0.98–0.78 (m, 6H). HRMS m/z : $[M + H]^+$ calc for $C_{21}H_{36}N_4NaO_{10}S_2$ 591.1770; found, 591.1647.

Sodium (2S)-2-((S)-2-(((6-tert-butoxycarbonyl)-6-azaspiro[3.4]octan-2-yl)oxy)carbonyl)amino)-4-methylpentanamido)-1-hydroxy-3-((R)-2-oxopyrrolidin-3-yl)propane-1-sulfonate (5c). Yield (22%). ¹H NMR (400 MHz, DMSO- d_6) δ 7.63 (s, 1H), 7.53 (s, 1H), 7.24–7.20 (m, 1H), 5.73–5.68 (m, 1H), 4.86–4.77 (m, 1H), 4.07–3.77 (m, 2H), 3.67–3.38 (m, 4H), 3.28–2.95 (m, 6H), 2.37–2.20 (m, 2H), 2.20–2.05 (m, 1H), 2.05–1.88 (m, 2H), 1.88–1.74 (m, 3H), 1.74–1.45 (m, 2H), 1.39 (s, 9H), 0.92–0.81 (m, 6H). HRMS m/z : $[M + Na]^+$ calc for $C_{26}H_{43}N_4Na_2O_{10}S$ 649.2496; found, 649.2458.

Sodium (2S)-2-((S)-2-(((2-tert-butoxycarbonyl)-2-azaspiro[3.4]octan-6-yl)oxy)carbonyl)amino)-4-methylpentanamido)-1-hydroxy-3-((R)-2-oxopyrrolidin-3-yl)propane-1-sulfonate (6c). Yield (7%). ¹H NMR (400 MHz, DMSO- d_6) δ 7.63–7.38 (m,

2H), 7.30–7.03 (m, 1H), 5.30 (dt, $J = 54.1, 5.9$ Hz, 1H), 5.00–4.81 (m, 1H), 4.66 (t, $J = 5.6$ Hz, 1H), 4.02–3.86 (m, 2H), 3.83–3.48 (m, 4H), 3.37–2.97 (m, 3H), 2.29–1.96 (m, 3H), 1.96–1.67 (m, 5H), 1.67–1.48 (m, 4H), 1.37 (s, 9H), 0.94–0.77 (m, 6H). HRMS m/z : $[M + Na]^+$ calc for $C_{26}H_{43}N_4Na_2O_{10}S$ 649.2496; found, 649.2454.

Sodium (2S)-2-((S)-2-(((7-(tert-butoxycarbonyl)-7-azaspiro[3.5]nonan-2-yl)oxy)carbonyl)amino)-4-methylpentanamido)-1-hydroxy-3-((R)-2-oxopyrrolidin-3-yl)propane-1-sulfonate (7c). Yield (87%). ¹H NMR (400 MHz, DMSO- d_6) δ 7.57–7.50 (m, 1H), 7.45 (s, 1H), 7.28 (dd, $J = 35.4, 8.4$ Hz, 1H), 5.33 (dd, $J = 56.7, 6.1$ Hz, 1H), 4.88–4.77 (m, 2H), 4.42–4.10 (m, 1H), 4.07–3.76 (m, 4H), 3.27–3.00 (m, 6H), 2.36–1.85 (m, 4H), 1.85–1.66 (m, 1H), 1.65–1.50 (m, 1H), 1.43 (d, $J = 14.3$ Hz, 6H), 1.38 (s, 9H), 0.89–0.79 (m, 6H). HRMS m/z : $[M + Na]^+$ calc for $C_{27}H_{45}N_4Na_2O_{10}S$ 663.2652; found, 663.2690.

Sodium (2S)-1-hydroxy-2-((S)-2-(((7-isobutyryl)-7-azaspiro[3.5]nonan-2-yl)oxy)carbonyl)amino)-4-methylpentanamido)-3-((R)-2-oxopyrrolidin-3-yl)propane-1-sulfonate (8c). Yield (80%). ¹H NMR (400 MHz, DMSO- d_6) δ 7.63 (s, 1H), 7.46 (s, 1H), 7.36–7.28 (m, 1H), 5.42 (dd, $J = 64.4, 6.1$ Hz, 1H), 4.87–4.81 (m, 1H), 4.52–4.12 (m, 2H), 4.09–3.80 (m, 2H), 3.22–2.97 (m, 4H), 2.88–2.79 (m, 2H), 2.37–2.18 (m, 3H), 2.18–1.96 (m, 1H), 1.96–1.68 (m, 3H), 1.68–1.32 (m, 8H), 1.00–0.94 (m, 6H), 0.92–0.80 (m, 6H). HRMS m/z : $[M + Na]^+$ calc for $C_{26}H_{43}N_4Na_2O_9S$ 633.2546; found, 633.2526.

Sodium (2S)-1-hydroxy-2-((S)-4-methyl-2-(((7-(2-phenylacetyl)-7-azaspiro[3.5]nonan-2-yl)oxy)carbonyl)amino)pentanamido)-3-((R)-2-oxopyrrolidin-3-yl)propane-1-sulfonate (9c). Yield (68%). ¹H NMR (400 MHz, DMSO- d_6) δ 7.60–7.49 (m, 2H), 7.45 (s, 1H), 7.35–7.11 (m, 5H), 5.38 (dd, $J = 60.0, 6.1$ Hz, 1H), 4.86–4.73 (m, 2H), 4.44–4.12 (m, 1H), 4.06–3.77 (m, 4H), 3.71–3.61 (m, 4H), 3.22–2.99 (m, 2H), 2.35–2.03 (m, 4H), 2.03–1.79 (m, 1H), 1.78–1.65 (m, 1H), 1.63–1.49 (m, 1H), 1.48–1.27 (m, 7H), 0.91–0.79 (m, 6H). HRMS m/z : $[M + Na]^+$ calc for $C_{30}H_{43}N_4Na_2O_9S$ 681.2546; found, 681.2522.

Sodium (2S)-1-hydroxy-2-((S)-4-methyl-2-(((7-(methylsulfonyl)-7-azaspiro[3.5]nonan-2-yl)oxy)carbonyl)amino)pentanamido)-3-((R)-2-oxopyrrolidin-3-yl)propane-1-sulfonate (10c). Yield (71%). ¹H NMR (400 MHz, DMSO- d_6) δ 7.62 (d, $J = 9.3$ Hz, 1H), 7.45 (s, 1H), 7.38–7.31 (m, 1H), 5.41 (dd, $J = 73.2, 6.1$ Hz, 1H), 4.88–4.76 (m, 1H), 4.28–3.76 (m, 2H), 3.21–2.91 (m, 6H), 2.83 (s, 3H), 2.35–1.98 (m, 3H), 1.96–1.68 (m, 4H), 1.67–1.50 (m, 6H), 1.49–1.32 (m, 2H), 1.14–1.01 (m, 1H), 0.91–0.78 (m, 6H). HRMS m/z : $[M + Na]^+$ calc for $C_{23}H_{39}N_4Na_2O_{10}S_2$ 641.1903; found, 641.1874.

Sodium (2S)-2-((S)-2-(((7-cyano-7-azaspiro[3.5]nonan-2-yl)oxy)carbonyl)amino)-4-methylpentanamido)-1-hydroxy-3-((R)-2-oxopyrrolidin-3-yl)propane-1-sulfonate (11c). Yield (74%). ¹H NMR (400 MHz, DMSO- d_6) δ 8.43 (d, $J = 7.6$ Hz, 1H), 7.63 (s, 1H), 7.30 (d, $J = 8.0$ Hz, 1H), 4.86–4.76 (m, 1H), 4.26–4.08 (m, 1H), 4.06–3.80 (m, 1H), 3.40–3.24 (m, 2H), 3.22–3.00 (m, 4H), 2.36–2.02 (m, 4H), 1.95–1.63 (m, 2H), 1.62–1.49 (m, 7H), 1.49–1.30 (m, 2H), 1.15–1.02 (m, 2H), 0.96–0.76 (m, 6H). HRMS m/z : $[M + H]^+$ calc for $C_{23}H_{37}N_5NaO_9S$ 566.2260; found, 566.2238.

Sodium (2S)-2-((S)-2-(((1-(tert-butoxycarbonyl)azetid-3-yl)oxy)carbonyl)amino)-4-methylpentanamido)-1-hydroxy-3-((R)-2-oxopyrrolidin-3-yl)propane-1-sulfonate (12c). Yield (64%). ¹H NMR (400 MHz, DMSO- d_6) δ 7.66 (d, $J = 11.1$ Hz, 2H), 7.58–7.42 (m, 1H), 5.01–4.90 (m, 2H), 4.71–4.64 (m, 1H), 4.23–3.84 (m, 3H), 3.84–3.51 (m, 2H), 3.19–3.04 (m, 2H), 2.34–2.01 (m, 2H), 2.00–1.73 (m, 1H), 1.71–1.43 (m, 5H), 1.38 (s, 9H), 0.92–0.81 (m, 6H). HRMS m/z : $[M + Na]^+$ calc for $C_{22}H_{37}N_4Na_2O_{10}S$ 595.2026; found, 595.1995.

Sodium (2S)-2-((S)-2-(((1-(tert-butoxycarbonyl)-3-methylazetid-3-yl)oxy)carbonyl)amino)-4-methylpentanamido)-1-hydroxy-3-((R)-2-oxopyrrolidin-3-yl)propane-1-sulfonate (13c). Yield (33%). ¹H NMR (400 MHz, DMSO- d_6) δ 7.64 (d, $J = 10.0$ Hz, 1H), 7.58–7.35 (m, 2H), 4.29–4.10 (m, 1H), 4.08–3.86 (m, 3H), 3.77–3.69 (m, 3H), 3.18–2.98 (m, 2H), 2.37–2.04 (m, 2H), 2.02–1.77 (m, 1H), 1.77–1.50 (m, 6H), 1.48–1.34 (m, 11H), 0.93–0.80 (m, 6H). HRMS m/z : $[M + Na]^+$ calc for $C_{23}H_{39}N_4Na_2O_{10}S$ 609.2183; found, 609.2160.

Sodium (2S)-2-((S)-2-(((1-(tert-butoxycarbonyl)azetidino-3-yl)methoxy)carbonyl)amino)-4-methylpentanamido)-1-hydroxy-3-((R)-2-oxopyrrolidin-3-yl)propane-1-sulfonate (14c). Yield (57%). ¹H NMR (400 MHz, DMSO-*d*₆) δ 7.59 (dd, *J* = 9.2, 5.5 Hz, 1H), 7.43 (s, 1H), 7.36–7.23 (m, 1H), 5.34 (dd, *J* = 69.8, 6.1 Hz, 1H), 4.14–4.01 (m, 2H), 4.01–3.76 (m, 3H), 3.62–3.47 (m, 2H), 3.20–2.98 (m, 3H), 2.87–2.67 (m, 1H), 2.24–2.06 (m, 3H), 2.04–1.80 (m, 1H), 1.72–1.48 (m, 3H), 1.46–1.39 (m, 1H), 1.37 (s, 9H), 0.92–0.80 (m, 6H). HRMS *m/z*: [M + Na]⁺ calc for C₂₃H₃₉N₄Na₂O₁₀S 609.2183; found, 609.2205.

Sodium (2S)-1-hydroxy-2-((S)-4-methyl-2-(((1-(2-phenylacetyl)azetidino-3-yl)methoxy)carbonyl)amino)pentanamido)-3-((R)-2-oxopyrrolidin-3-yl)propane-1-sulfonate (15c). Yield (92%). ¹H NMR (400 MHz, DMSO-*d*₆) δ 8.16 (s, 1H), 7.64 (s, 1H), 7.52–7.44 (m, 1H), 7.34–7.14 (m, 5H), 4.22 (d, *J* = 6.5 Hz, 2H), 4.14–3.79 (m, 4H), 3.72–3.54 (m, 2H), 3.50–3.38 (m, 2H), 3.23–3.00 (m, 4H), 2.38–1.95 (m, 3H), 1.93–1.72 (m, 1H), 1.72–1.53 (m, 2H), 1.53–1.30 (m, 2H), 0.92–0.80 (m, 6H). HRMS *m/z*: [M + H]⁺ calc for C₂₆H₃₈N₄NaO₉S 605.2257; found, 605.2698.

Sodium (2S)-2-((2S)-2-(((1-(bicyclo[2.2.1]heptane-2-carbonyl)azetidino-3-yl)methoxy)carbonyl)amino)-4-methylpentanamido)-1-hydroxy-3-((R)-2-oxopyrrolidin-3-yl)propane-1-sulfonate (16c). Yield (71%). ¹H NMR (400 MHz, DMSO-*d*₆) δ 7.78 (s, 1H), 7.64 (s, 1H), 7.38 (s, 1H), 4.18 (s, 1H), 4.13–3.79 (m, 3H), 3.72–3.54 (m, 2H), 3.26–2.96 (m, 4H), 2.70–2.55 (m, 1H), 2.36–2.02 (m, 4H), 2.00–1.76 (m, 1H), 1.75–1.32 (m, 9H), 1.29–1.19 (m, 4H), 1.19–1.00 (m, 2H), 0.93–0.77 (m, 6H). HRMS *m/z*: [M + H]⁺ calc for C₂₆H₄₂N₄NaO₉S 609.2570; found, 609.3013.

Sodium (2S)-1-hydroxy-2-((S)-4-methyl-2-(((1-(methylsulfonyl)azetidino-3-yl)methoxy)carbonyl)amino)pentanamido)-3-((R)-2-oxopyrrolidin-3-yl)propane-1-sulfonate (17c). Yield (88%). ¹H NMR (400 MHz, DMSO-*d*₆) δ 7.64 (s, 1H), 7.16 (s, 1H), 6.96 (s, 1H), 4.67 (s, 2H), 4.29–3.83 (m, 5H), 3.81–3.52 (m, 3H), 3.24–2.96 (m, 2H), 2.36–2.02 (m, 2H), 1.95–1.73 (m, 1H), 1.59 (s, 4H), 1.37 (s, 3H), 1.24 (s, 1H), 0.97–0.77 (m, 6H). HRMS *m/z*: [M + H]⁺ calc for C₁₉H₃₄N₄NaO₁₀S₂ 565.1614; found, 565.1878.

Sodium (2S)-2-((S)-2-(((1-(tert-butoxycarbonyl)azetidino-3-yl)methoxy-*d*2)carbonyl)amino)-4-methylpentanamido)-1-hydroxy-3-((R)-2-oxopyrrolidin-3-yl)propane-1-sulfonate (18c). Yield (71%). ¹H NMR (400 MHz, dmso) δ 7.68–7.56 (m, 1H), 7.50–7.42 (m, 1H), 7.39–7.23 (m, 1H), 5.42 (dd, *J* = 73.8, 6.2 Hz, 1H), 4.28–3.96 (m, 2H), 3.94–3.75 (m, 2H), 3.68–3.50 (m, 2H), 3.16–3.00 (m, 2H), 2.83–2.70 (m, 1H), 2.27–1.80 (m, 4H), 1.66–1.47 (m, 2H), 1.47–1.40 (m, 2H), 1.37 (s, 9H), 0.93–0.80 (m, 6H). HRMS *m/z*: [M + Na]⁺ calc for C₂₃H₃₇D₂N₄Na₂O₁₀S 611.2308; found, 611.2258.

Biochemical Studies. Enzyme Assays and Inhibition Studies. Cloning and Expression of the 3CL Protease of SARS-CoV-2 and FRET Enzyme Assays. The codon-optimized cDNA of full length of 3CL^{pro} of SARS-CoV-2 (GenBank number MN908947.3) fused with sequences encoding 6 histidine at the N-terminal was synthesized by Integrated DNA (Coralville, IA). The synthesized gene was subcloned into the pET-28a(+) vector. The expression and purification of SARS-CoV-2 3CL^{pro} were conducted following a standard procedure described previously.^{23,28,29}

Briefly, a stock solution of an inhibitor was prepared in DMSO and diluted in assay buffer composed of 20 mM HEPES buffer, pH 8, containing NaCl (200 mM), EDTA (0.4 mM), glycerol (60%), and 6 mM dithiothreitol (DTT). The SARS-CoV-2 protease was mixed with serial dilutions of inhibitors 1–18b/c or with DMSO in 25 μL of assay buffer and incubated at 37 °C for 1 h, followed by the addition of 25 μL of assay buffer containing substrate (FAM-SAVLQ/SG-QXL520, AnaSpec, Fremont, CA). The substrate was derived from the cleavage sites on the viral polyproteins of SARS-CoV. Fluorescence readings were obtained using an excitation wavelength of 480 nm and an emission wavelength of 520 nm on a fluorescence microplate reader (FLx800; Biotec, Winooski, VT) 1 h following the addition of substrate. Relative fluorescence units (RFU) were determined by subtracting background values (substrate-containing well without protease) from the raw fluorescence values, as described previously.²⁹ The dose-dependent FRET inhibition curves were fitted with a variable slope using GraphPad Prism software (GraphPad, La

Jolla, CA) to determine the IC₅₀ values of the compounds. To assess if the compounds have a broad-spectrum activity to other coronaviruses, they were also examined against MERS-CoV 3CL^{pro} as described before.²³

Antiviral Assays/Cell-Based Inhibition Assays. To assess antiviral effects of selected compounds (dissolved in DMSO) in cell culture, the SARS-CoV-2 replicon system with pSMART-T7-scv2-replicon (pSMART BAC V2.0 Vector Containing the SARS-CoV-2, Wuhan-Hu-1 Non-Infectious Replicon) was used.⁴⁶ The synthetic SARS-CoV-2 replicon RNA was prepared from the pSMART-T7-scv2-replicon as described,⁴⁷ and the Neon Electroporation system (ThermoFisher, Chicago, IL) was used for the RNA electroporation to 293T cells. After the electroporation, the cells were incubated with DMSO (0.1%) or each compound at 2, 0.5, 0.1, and 0.02 μM for 30 h, and luciferase activities were measured for antiviral effects. The dose-dependent inhibition curve for each compound was prepared, and the 50% effective concentration (EC₅₀) values were determined by GraphPad Prism software using a variable slope (GraphPad, La Jolla, CA).

Nonspecific Cytotoxic Effects/Measurement of In Vitro Cytotoxicity. Confluent cells grown in 96-well plates were incubated with various concentrations (1–100 μM) of each compound for 72 h. Cell cytotoxicity was measured by a CytoTox 96 nonradioactive cytotoxicity assay kit (Promega, Madison, WI), and the CC₅₀ values were calculated using a variable slope by GraphPad Prism software. The *in vitro* safety index was calculated by dividing the CC₅₀ by the EC₅₀.

X-ray Crystallographic Studies. Crystallization and Data Collection. Purified MERS-CoV 3CL^{pro} and SARS-CoV-2 3CL^{pro} in 100 mM NaCl and 20 mM Tris pH 8.0 were concentrated to 10 mg/mL (0.3 mM) for crystallization screening. Stock solutions of the inhibitors were prepared in DMSO at 100 mM, and the complexes with the 3CL proteases were prepared by adding 2 mM of each compound and incubating the complexes on ice for 1 h. All crystallization experiments were setup using an NT8 drop-setting robot (Formulatrix, Inc.) and UVXPO MRC (Molecular Dimensions) sitting drop vapor diffusion plates at 18 °C. Protein (100 nL) and crystallization solution (100 nL) were dispensed and equilibrated against 50 μL of the latter. Crystals of the MERS-CoV 3CL^{pro} complexes were obtained from the following conditions. Index HT screen (Hampton Research) 9c: condition E7 (30% (w/v) PEG 550 MME, 100 mM Hepes pH 7.5, 50 mM magnesium chloride), 8c: condition F7 (20% (w/v) PEG 3350, 100 mM Bis-Tris pH 6.5, 200 mM ammonium sulfate) and 10c: condition F5 (17% (w/v) PEG 10000, 100 mM Bis-Tris pH 5.5, 100 mM ammonium acetate). Proplex HT screen (Molecular Dimensions) 14c: condition E2 (25% (w/v) PEG 3350, 100 mM Hepes pH 7.5, 200 mM magnesium chloride). Crystals of the SARS-CoV-2 3CL^{pro} complexes were obtained from the following conditions. PACT screen (Molecular Dimensions) 2c: condition C2 (25% (w/v) PEG 1500, 100 mM PCTP pH 5.0), 3c: condition C1 (25% (w/v) PEG 1500, 100 mM PCTP pH 4.0), 11c: condition E1 (20% (w/v) PEG 3350, 20 mM sodium/postassium phosphate) and 10c: condition D4 (25% (w/v) PEG 1500, 100 mM MMT pH 7.0), Index HT screen (Hampton Research) 4c: condition F5 (17% (w/v) PEG 10000, 100 mM Bis-Tris pH 5.5, 100 mM ammonium acetate), 8c: condition F10 (25% (w/v) PEG 3350, 100 mM Bis-Tris pH 5.5, 200 mM NaCl), 14c: condition F11 (25% (w/v) PEG 3350, 100 mM Bis-Tris pH 6.5, 200 mM sodium chloride), 9c: condition G4 (20% (w/v) PEG 3350, 100 mM Hepes pH 7.5, 200 mM lithium sulfate) and Berkeley screen (Rigaku Reagents) 7c: condition B6 (20% (w/v) PEG 3350, 200 mM sodium fluoride). Cryoprotectants containing 80% crystallant and 20% (v/v) PEG 200 were layered onto the drop, the samples were harvested and stored in liquid nitrogen. For MERS-CoV 3CL^{pro} in complex with 9c, the crystallization solution served as the cryoprotectant. X-ray diffraction data were collected at the Advanced Photon Source beamline 17-ID (IMCA-CAT) and National Synchrotron Light Source-II, beamline 19-ID (NYX).

Structure Solution and Refinement. Intensities were integrated using XDS^{48,49} via Autoproc⁵⁰ and the Laue class analysis and data

scaling were performed with Aimless.⁵¹ Structure solution was conducted by molecular replacement with Phaser⁵² using a previously determined inhibitor bound structures of MERS-CoV (SWKK) and SARS-CoV-2 3CL^{pro} (PDB 6XMK) as the search models. Structure refinement and manual model building were conducted with Phenix⁵³ and Coot,⁵⁴ respectively. Disordered side chains were truncated to the point for which electron density could be observed. Structure validation was conducted with Molprobit,⁵⁵ and figures were prepared using the CCP4MG package.⁵⁶ Crystallographic data are provided in Tables S1 and S2.^{57–61}

■ ASSOCIATED CONTENT

SI Supporting Information

The Supporting Information is available free of charge at <https://pubs.acs.org/doi/10.1021/acs.jmedchem.2c00224>.

Comparison of **14c** bound to MERS-CoV 3CL^{pro} and SARS-CoV-2 3CL^{pro}; comparison of azaspiro [3.3] inhibitors **2c**, **3c**, and **4c** bound to SARS-CoV-2 3CL^{pro}; binding modes of azaspiro [3.5] inhibitors **7c** and **11c** with SARS-CoV-2 3CL^{pro}; comparison of azaspiro [3.5] inhibitors **7c**, **8c**, **11c**, **10c**, and **9c** bound to SARS-CoV-2 3CL^{pro}; comparison of azaspiro [3.5] inhibitors **8c**, **9c**, and **10c** with MERS-CoV 3CL^{pro}; crystallographic data for SARS-CoV-2 3CL^{pro} inhibitor complexes; crystallographic data for MERS-CoV 3CL^{pro} inhibitor complexes; and absolute qNMR data (PDF) Molecular formula strings—SMILES codes (CSV) PDB validation reports for new X-ray crystal structures (ZIP)

Accession Codes

Coordinates and structure factors for complexes with the following with inhibitors were deposited to the Worldwide Protein Databank (wwPDB) with the accession codes: MERS-CoV 3CL^{pro} complexes: **8c** (7T3Y), **9c** (7T3Z), **10c** (7T40), **14c** (7T41) and SARS-CoV-2 3CL^{pro} complexes: **2c** (7T42), **3c** (7T43), **4c** (7T44), **7c** (7T45), **8c** (7T46), **9c** (7T48), **10c** (7T49), **11c** (7T4A), **14c** (7T4B). The authors will release the atomic coordinates upon article publication.

■ AUTHOR INFORMATION

Corresponding Authors

Kyeong-Ok Chang – Department of Diagnostic Medicine & Pathobiology, College of Veterinary Medicine, Kansas State University, Manhattan, Kansas 66506, United States; Phone: (316) 978 7374; Email: kchang@vet.ksu.edu

William C. Groutas – Department of Chemistry and Biochemistry, Wichita State University, Wichita, Kansas 67260, United States; orcid.org/0000-0001-5248-7912; Phone: (785) 532 3849; Email: bill.groutas@wichita.edu

Authors

Chamandi S. Dampalla – Department of Chemistry and Biochemistry, Wichita State University, Wichita, Kansas 67260, United States; orcid.org/0000-0002-8199-2376

Athri D. Rathnayake – Department of Chemistry and Biochemistry, Wichita State University, Wichita, Kansas 67260, United States; orcid.org/0000-0003-2588-7624

Anushka C. Galasiti Kankanamalage – Department of Chemistry and Biochemistry, Wichita State University, Wichita, Kansas 67260, United States

Yunjeong Kim – Department of Diagnostic Medicine & Pathobiology, College of Veterinary Medicine, Kansas State University, Manhattan, Kansas 66506, United States

Krishani Dinali Perera – Department of Diagnostic Medicine & Pathobiology, College of Veterinary Medicine, Kansas State University, Manhattan, Kansas 66506, United States;

orcid.org/0000-0002-3778-4975

Harry Nhat Nguyen – Department of Chemistry and Biochemistry, Wichita State University, Wichita, Kansas 67260, United States

Matthew J. Miller – Department of Chemistry and Biochemistry, Wichita State University, Wichita, Kansas 67260, United States

Trent K. Madden – Department of Chemistry and Biochemistry, Wichita State University, Wichita, Kansas 67260, United States

Hunter R. Picard – Department of Chemistry and Biochemistry, Wichita State University, Wichita, Kansas 67260, United States

Hayden A. Thurman – Department of Chemistry and Biochemistry, Wichita State University, Wichita, Kansas 67260, United States

Maithri M. Kashipathy – Protein Structure Laboratory, The University of Kansas, Lawrence, Kansas 66047, United States

Lijun Liu – Protein Structure Laboratory, The University of Kansas, Lawrence, Kansas 66047, United States

Kevin P. Battaile – NYX, New York Structural Biology Center, Upton, New York 11973, United States; orcid.org/0000-0003-0833-3259

Scott Lovell – Protein Structure Laboratory, The University of Kansas, Lawrence, Kansas 66047, United States

Complete contact information is available at:

<https://pubs.acs.org/doi/10.1021/acs.jmedchem.2c00224>

Notes

The authors declare no competing financial interest.

■ ACKNOWLEDGMENTS

This research was supported in part by grants from the National Institutes of Health (NIH) (grants R01 AI109039 and AI161085 to K.O.C). Use of the IMCA-CAT beamline 17-ID at the Advanced Photon Source was supported by the companies of the Industrial Macromolecular Crystallography Association through a contract with Hauptman-Woodward Medical Research Institute. Use of the Advanced Photon Source was supported by the U.S. Department of Energy, Office of Science, Office of Basic Energy Sciences under contract no. DE-AC02-06CH11357. This research used the Biological Microdiffraction Facility beamline 19-ID (NYX) at the National Synchrotron Light Source II, a U.S. Department of Energy (DOE) Office of Science User Facility operated for the DOE Office of Science by Brookhaven National Laboratory under Contract No. DE-SC0012704. Support for the NMR instrumentation was provided by NIH Shared Instrumentation Grant # S10RR024664 and NSF Major Research Instrumentation Award # 1625923. Use of the University of Kansas Protein Structure Laboratory was supported by a grant from the National Institute of General Medical Sciences (P30GM110761) of the NIH. The Center for BioMolecular Structure (CBMS) is primarily supported by the National Institutes of Health, National Institute of General Medical Sciences (NIGMS) through a Center Core P30 Grant (P30GM133893) and by the DOE Office of Biological and Environmental Research (KP1605010). The following reagent was obtained through BEI Resources, NIAID, NIH: pSMART

BAC V2.0 Vector Containing the SARS-Related Coronavirus-2, Wuhan-Hu-1 Non-Infectious Replicon, NR-54972.

ABBREVIATIONS USED

CC₅₀, 50% cytotoxic concentration in cell-based assays; CDI, carbonyl diimidazole; CPE, cytopathic effects; DMSO, dimethyl sulfoxide; DMP, Dess–Martin periodinane; DSC, *N,N'*-disuccinimidyl carbonate; DTT, dithiothreitol; EC₅₀, 50% effective concentration in cell culture; GESAMT, general efficient structural alignment of macromolecular targets; IC₅₀, 50% inhibitory concentration in the enzyme assay; MME, monomethyl ether; MNV, murine norovirus; MOI, multiplicity of infection; ORF, open reading frame; PK, pharmacokinetics; RMSD, root-mean-square deviation; TCID₅₀, 50% tissue culture infectious dose; TEA, triethyl amine; XDS, X-ray detector software

REFERENCES

- (1) Perlman, S.; Masters, P. S. *Coronaviridae: The Viruses and Their Replication*. In *Fields Virology: Emerging Viruses*; Howley, P. M.; Knipe, D. M.; Whelan, S., Eds.; Wolters Kluwer: Wichita, 2020; Vol. 1, pp 410–448.
- (2) Wu, F.; Zhao, S.; Yu, B.; Chen, Y.-M.; Wang, W.; Song, Z.-G.; Hu, Y.; Tao, Z.-W.; Tian, J.-H.; Pei, Y.-Y.; Yuan, M.-L.; Zhang, Y.-L.; Dai, F.-H.; Liu, Y.; Wang, Q.-M.; Zheng, J.-J.; Xu, L.; Holmes, E. C.; Zhang, Y.-Z. A new coronavirus associated with human respiratory disease in China. *Nature* **2020**, *579*, 265–269.
- (3) Zhu, N.; Zhang, D.; Wang, W.; Li, X.; Yang, B.; Song, J.; Zhao, X.; Huang, B.; Shi, W.; Lu, R.; Niu, P.; Zhan, F.; Ma, X.; Wang, D.; Xu, W.; Wu, G.; Gao, G. F.; Tan, W. A novel coronavirus from patients with pneumonia in China. *N. Engl. J. Med.* **2020**, *382*, 727–733.
- (4) Hu, B.; Guo, H.; Zhou, P.; Shi, Z.-L. Characteristics of SARS-CoV-2 and COVID-19. *Nat. Rev. Microbiol.* **2021**, *19*, 141–154.
- (5) Harrison, A. G.; Lin, T.; Wang, P. Mechanisms of SARS-CoV-2 transmission and pathogenesis. *Trends Immunol.* **2020**, *41*, 1100–1115.
- (6) Ghosh, A. K.; Brindisi, M.; Shahabi, D.; Chapman, M. E.; Mesecar, A. D. Drug development and medicinal chemistry efforts toward SARS-Coronavirus and Covid-19 therapeutics. *Chem. Med. Chem.* **2020**, *15*, 907–932.
- (7) Gil, C.; Ginex, T.; Maestro, I.; Nozal, V.; Barrado-Gil, L.; Cuesta-Geijo, M. A.; Urquiza, J.; Ramirez, D.; Alonso, C.; Campillo, N. E.; Martinez, A. COVID-19: Drug targets and potential treatments. *J. Med. Chem.* **2020**, *63*, 12359–12386.
- (8) Sharma, A.; Tiwari, S.; Deb, M. K.; Marty, J. L. Severe Acute Respiratory Syndrome Coronavirus-2 (SARS-CoV-2): A global pandemic and treatments strategies. *Int. J. Antimicrob. Agents* **2020**, *56*, No. 106054.
- (9) Cannalire, R.; Cerchia, C.; Beccari, A. R.; Di Leva, F. S.; Summa, V. Targeting SARS-CoV-2 proteases and polymerase for COVID-19 treatment: State of the art and future opportunities. *J. Med. Chem.* **2022**, *65*, 2716–2746.
- (10) Yoshimoto, F. K. The proteins of Severe Acute Respiratory Coronavirus-2 (SARS-CoV-2 or nCOVID-19), the cause of COVID-19. *Protein J.* **2020**, *39*, 198–216.
- (11) Hirano, T.; Murakami, M. COVID-19: a new virus, but a familiar receptor and cytokine release syndrome. *Immunity* **2020**, *52*, 731–733.
- (12) Tai, W.; He, L.; Zhang, X.; Pu, J.; Voronin, D.; Jiang, S.; Zhou, Y.; Du, L. Characterization of the receptor binding domain (RBD) of 2019 novel coronavirus: implication for development of RBD protein as a viral attachment inhibitor and vaccine. *Cell. Mol. Immunol.* **2020**, *17*, 613–620.
- (13) Cheng, Y.-W.; Chao, T.-L.; Li, C.-L.; Chiu, M.-F.; Kao, H.-C.; Wang, S.-H.; Pang, Y.-H.; Lin, C.-H.; Tsai, Y.-M.; Lee, W.-H.; Tao, M.-H.; Ho, T.-C.; Wu, P.-Y.; Jang, L.-T.; Chen, P.-J.; Chang, S.-Y.; Yeh, S.-H. Furin inhibitors block SARS-CoV-2 spike protein cleavage to suppress virus production and cytopathic effects. *Cell Rep.* **2020**, *33*, No. 108254.
- (14) The nomenclature used is that of Schechter, I. and Berger, A.. On the size of the active site in proteases. I. Papain. *Biochem. Biophys. Res. Com.* **2012**, *425*, 497–502. where the residues on the N-terminus side of the peptide bond that is cleaved are designated as P₁-P_n and those on the C-terminus side are designated P₁'-P_n'. The corresponding active site subsites are designated S₁-S_n and S₁'-S_n'. P₁ is the primary substrate specificity residue and P₁-P₁' is the scissile bond
- (15) Rut, W.; Groborz, K.; Zhang, L.; Sun, X.; Zmudzinski, M.; Pawlik, B.; Wang, X.; Jochmans, D.; Neyts, J.; Mlynarski, W.; Hilgenfeld, R.; Drag, M. M. SARS-CoV-2 M^{pro} inhibitors and activity-based probes for patient-sample imaging. *Nat. Chem. Biol.* **2021**, *17*, 222–228.
- (16) Zhang, L.; Lin, D.; Sun, X.; Curth, U.; Drosten, C.; Sauerhering, L.; Becker, S.; Rox, K.; Hilgenfeld, R. Crystal structure of SARS-CoV-2 main protease provides a basis for design of improved α -ketoamide inhibitors. *Science* **2020**, *368*, 409–412.
- (17) Jin, Z.; Du, X.; Xu, Y.; Deng, Y.; Liu, M.; Zhao, Y.; Zhang, B.; Li, X.; Zhang, L.; Peng, C.; Duan, Y.; Yu, J.; Wang, L.; Yang, K.; Liu, F.; Jiang, R.; Yang, X.; You, T.; Liu, X.; Yang, X.; Bai, F.; Liu, H.; Liu, X.; Guddat, L. W.; Xu, W.; Xiao, G.; Qin, C.; Shi, Z.; Jiang, H.; Rao, Z.; Yang, H. Structure of M pro from SARS-CoV-2 and discovery of its inhibitors. *Nature* **2020**, *582*, 289–293.
- (18) Dai, W.; Zhang, B.; Jiang, X.-M.; Su, H.; Li, J.; Zhao, Y.; Xie, X.; Jin, Z.; Peng, J.; Liu, F.; Li, C.; Li, Y.; Bai, F.; Wang, H.; Cheng, X.; Cen, X.; Hu, S.; Yang, X.; Wang, J.; Liu, X.; Xiao, G.; Jiang, H.; Rao, Z.; Zhang, L.-K.; Xu, Y.; Yang, H.; Liu, H. Structure-based design of antiviral drug candidates targeting the SARS-CoV-2 main protease. *Science* **2020**, *368*, 1331–1335.
- (19) Ullrich, S.; Nitsche, C. The SARS-CoV-2 main protease as drug target. *Bioorg. Med. Chem. Lett.* **2020**, *30*, No. 127377.
- (20) He, J.; Hu, L.; Huang, X.; Wang, C.; Zhang, Z.; Wang, Y.; Zhang, D.; Ye, W. Potential of coronavirus 3C-like protease inhibitors for the development of new anti-SARS-CoV-2 drugs: Insights from structures of protease and inhibitors. *Int. J. Antimicrob. Agents* **2020**, *56*, No. 106055.
- (21) Rut, W.; Lv, Z.; Zmudzinski, M.; Patchett, S.; Nayak, D.; Snipas, S. J.; El Oualid, F.; Huang, T. T.; Bekes, M.; Drag, M.; Olsen, S. K. Activity profiling and crystal structures of inhibitor-bound SARS-CoV-2 papain-like protease: A framework for anti-COVID-19 drug design. *Sci. Adv.* **2020**, *6*, No. eabd4596.
- (22) Banerjee, R.; Perera, L.; Tillekeratne, L.M.V. Potential SARS-CoV-2 main protease inhibitors. *Drug Discovery Today* **2021**, *26*, 804–816.
- (23) Rathnayake, A. D.; Zheng, J.; Kim, Y.; Perera, K. D.; Mackin, S.; Meyerholz, D. K.; Kashipathy, M. M.; Battaile, K. P.; Lovell, S.; Perlman, S.; et al. 3C-like protease inhibitors block coronavirus replication in vitro and improve survival in MERS-CoV-infected mice. *Sci. Transl. Med.* **2020**, *12*, No. eabc5332.
- (24) Dampalla, C. S.; Kim, Y.; Bickmeier, N.; Rathnayake, A. D.; Nguyen, H. N.; Zheng, J.; Kashipathy, M. M.; Baird, M. A.; Battaile, K. P.; Lovell, S.; Perlman, S.; Chang, K. O.; Groutas, W. C. Structure-guided design of conformationally-constrained cyclohexane inhibitors of severe acute respiratory syndrome coronavirus-2 3CL protease. *J. Med. Chem.* **2021**, *64*, 10047–10058.
- (25) Dampalla, C. S.; Rathnayake, A. D.; Perera, K. D.; Jesri, A.-R. M.; Nguyen, H. N.; Miller, M. J.; Thurman, H. A.; Zheng, J.; Kashipathy, M. M.; Battaile, K. P.; Lovell, S.; Perlman, S.; Kim, Y.; Groutas, W. C.; Chang, K. O. Structure-guided design of potent inhibitors of SARS-CoV-2 3CL protease: structural, biochemical, and cell-based studies. *J. Med. Chem.* **2021**, *64*, 17846–17865.
- (26) Dampalla, C. S.; Zheng, J.; Perera, K. D.; Wong, L.-Y. R.; Meyerholz, D. K.; Nguyen, H. N.; Kashipathy, M. M.; Battaile, K. P.; Lovell, S.; Kim, Y.; Perlman, S.; Groutas, W. C.; Chang, K.-O. Post-infection treatment with a protease inhibitor increases survival of mice

with a fatal SARS-CoV-2 infection. *Proc. Natl. Acad. Sci. U.S.A.* **2021**, *118*, No. e2101555118.

(27) Pedersen, N. C.; Kim, Y.; Liu, H.; Galasiti Kankanamalage, A. C.; Eckstrand, C.; Groutas, W. C.; Bannasch, M.; Meadows, J. M.; Chang, K.-O. Efficacy of a 3C-like protease inhibitor in treating various forms of acquired feline infectious peritonitis. *J. Feline Med. Surg.* **2018**, *20*, 378–392.

(28) Kim, Y.; Liu, H.; Galasiti Kankanamalage, A. C.; Weerasekara, S.; Hua, D. H.; Groutas, W. C.; Chang, K.-O.; Pedersen, N. C. Reversal of the progression of fatal coronavirus infection in cats by a broad-spectrum coronavirus protease inhibitor. *PLoS Pathog.* **2016**, *12*, No. e1005531.

(29) Kim, Y.; Lovell, S.; Tiew, K.-C.; Mandadapu, S. R.; Alliston, K. R.; Battaile, K. P.; Groutas, W. C.; Chang, K.-O. Broad-spectrum antivirals against 3C or 3C-like proteases of picornaviruses, noroviruses, and coronaviruses. *J. Virol.* **2012**, *86*, 11754–11762.

(30) Qiao, J.; Li, Y.-S.; Zeng, R.; Liu, F.-L.; Luo, R.-H.; Huang, C.; Wang, Y.-F.; Zhang, J.; Quan, B.; Shen, C.; Mao, X.; Liu, X.; Sun, W.; Yang, W.; Ni, X.; Wang, K.; Xu, L.; Duan, Z.-L.; Zou, Q.-C.; Zhang, H.-L.; Qu, W.; Long, Y.-H.-P.; Li, M.-H.; Yang, R.-C.; Liu, X.; You, J.; Zhou, Y.; Yao, R.; Li, W.-P.; Liu, J.-M.; Chen, P.; Liu, Y.; Lin, G.-F.; Yang, X.; Zou, J.; Li, L.; Hu, Y.; Lu, G.-W.; Li, W.-M.; Wei, Y.-Q.; Zheng, Y.-T.; Lei, J.; Yang, S. SARS-CoV-2 M^{pro} inhibitors with antiviral activity in a transgenic mouse model. *Science* **2021**, *371*, 1374–1378.

(31) Bai, B.; Belovodskiy, A.; Hena, M.; Kandadai, A. S.; Joyce, M. A.; Saffran, H. A.; Shields, J. A.; Khan, M. B.; Arutyunova, E.; Lu, J.; Bajwa, S. K.; Hockman, D.; Fischer, C.; Lamer, T.; Vuong, W.; van Belkum, M. J.; Gu, Z.; Lin, F.; Du, Y.; Xu, J.; Rahim, M.; Young, H. S.; Vederas, J. C.; Tyrrell, D. L.; Lemieux, M. J.; Nieman, J. A. Peptidomimetic α -acyloxymethylketone warheads with six-membered lactam P1 glutamine mimic: SARS-CoV-2 3CL protease inhibition, coronavirus antiviral activity, and in vitro biological stability. *J. Med. Chem.* **2021**, *65*, 2905–2925.

(32) Ghosh, A. K.; Raghavaiah, J.; Shahabi, D.; Yadav, M.; Anson, B. J.; Lendy, E. K.; Hattori, S.; Higashi-Kuwata, N.; Mitsuya, H.; Mesecar, A. D. Indole chloropyridinyl ester-derived SARS-CoV-2 3CLpro inhibitors: enzyme inhibition, antiviral efficacy, structure-activity relationship and X-ray structural studies. *J. Med. Chem.* **2021**, *64*, 14702–14714.

(33) Konno, S.; Kobayashi, K.; Senda, M.; Funai, Y.; Seki, Y.; Tamai, I.; Schakel, L.; Sakata, K.; Pillaiyar, T.; Taguchi, A.; Taniguchi, A.; Gutschow, M.; Muller, C. E.; Takeuchi, K.; Hirohama, M.; Kawaguchi, A.; Kojima, M.; Senda, T.; Shirasaka, Y.; Kamitani, W.; Hayashi, Y. 3CL protease inhibitors with an electrophilic acylketone moiety as anti-SARS-CoV-2 agents. *J. Med. Chem.* **2021**, *65*, 2926–2939.

(34) Li, L.; Chenna, B. C.; Yang, K. S.; Cole, T. R.; Goodall, Z. T.; Giardini, M.; Moghadamchargari, Z.; Hernandez, E. A.; Gomez, J.; Calvet, C. M.; Bernatchez, J. A.; Mellott, D. M.; Zhu, J.; Rademacher, A.; Thomas, D.; Blankenship, L. R.; Drelich, A.; Laganowsky, A.; Tseng, C.-T. K.; Liu, W. R.; Wand, A. J.; Cruz-Reyes, J.; Siqueira-Neto, J.; Meek, T. D. Self-masked aldehyde inhibitors: a novel strategy for inhibiting cysteine proteases. *J. Med. Chem.* **2021**, *64*, 11267–11287.

(35) Han, S. H.; Goins, C. M.; Arya, T.; Shin, W.-J.; Maw, J.; Hooper, A.; Sonawane, D. P.; Porter, M. R.; Bannister, B. E.; Crouch, R. D.; Lindsey, A. A.; Lakatos, G.; Martinez, S. R.; Alvarado, J.; Akers, W. S.; Wang, N. S.; Jung, J. U.; Macdonald, J. D.; Stauffer, S. R. Structure-based optimization of ML300-derived, noncovalent inhibitors targeting the Severe Acute Respiratory Syndrome Coronavirus 3CL protease (SARS-CoV-3CL^{pro}). *J. Med. Chem.* **2022**, *65*, 2880–2904.

(36) Breidenbach, J.; Lemke, C.; Pillaiyar, T.; Schakel, L.; Al Hamwi, G.; Dieltz, M.; Gedtschold, R.; Geiger, N.; Lopez, V.; Mirza, S.; Namasivayam, V.; Schiedel, A. C.; Sylvester, K.; Thimm, D.; Vielmuth, C.; Vu, L. P.; Zylulina, M.; Bodem, J.; Gutschow, M.; Muller, C. E. Targeting the main protease of SARS-CoV-2: from the

establishment of a high throughput screening to the design of tailored inhibitors. *Angew. Chem., Int. Ed.* **2021**, *60*, 10423–10429.

(37) Deshmukh, M. G.; Ippolito, J. A.; Zhang, C.-H.; Stone, E. A.; Reilly, R. A.; Miller, S. J.; Jorgensen, W. L.; Anderson, K. S. Structure-guided design of a perampanel-derived pharmacophore targeting the SARS-CoV-2 main protease. *Structure* **2021**, *29*, 823–833.

(38) Owen, D. R.; Allerton, C. M. N.; Anderson, A. S.; Aschenbrenner, L.; Avery, M.; Berritt, S.; Boras, B.; Cardin, R. D.; Carlo, A.; Coffman, K. J.; Dantonio, A.; Di, L.; Eng, H.; Ferre, R.; Gajiwala, K. S.; Gibson, S. A.; Greasley, S. E.; Hurst, B. L.; Kadar, E. P.; Kalgutkar, A. S.; Lee, J. C.; Lee, J.; Liu, W.; Mason, S. W.; Noell, S.; Novak, J. J.; Obach, R. S.; Ogilvie, K.; Patel, N. C.; Pettersson, M.; Rai, D. K.; Reese, M. R.; Sammons, M. F.; Sathish, J. G.; Singh, R.S.P.; Steppan, C. M.; Stewart, A. E.; Tuttle, J. B.; Updyke, L.; Verhoest, P. R.; Wei, L.; Yang, Q.; Zhu, Y. An oral SARS-CoV-2 M^{pro} inhibitor clinical candidate for the treatment of COVID-19. *Science* **2021**, *374*, 1586–1593.

(39) Boras, B.; Jones, R. M.; Anson, B. J.; Arenson, D.; Aschenbrenner, L.; Bakowski, M. A.; Beutler, N.; Binder, J.; Chen, E.; Eng, H. J.; Haupt, R. E.; E, P.; Kania, R.; Kimoto, E.; Kirkpatrick, M. G.; Lanyon, L.; Lendy, E. K.; Marra, M. T.; Logue, J.; Luthra, S. A.; Ma, C.; Mason, S. W.; McGrath, M. E.; Noell, S.; Obach, R. S.; O'Brien, M. N.; O'Connor, R.; Ogilvie, K.; Owen, D.; Pettersson, M.; Reese, M. R.; Rogers, T. F.; Rosales, R.; Rossulek, M. I.; Sathish, J. G.; Shirai, N.; Steppan, C.; Ticehurst, M.; Updyke, L. W.; Weston, S.; Zhu, Y.; White, K. M.; Garcia-Sastre, A.; Wang, J.; Chatterjee, A. K.; Mesecar, A. D.; Frieman, M. B.; Anderson, A. S.; Allerton, C.; et al. Preclinical characterization of an intravenous coronavirus 3CL protease inhibitor for the potential treatment of COVID 19. *Nat. Commun.* **2021**, *12*, No. 6055.

(40) Hoffman, R. L.; Kania, R. S.; Brothers, M. A.; Davies, J. F.; Ferre, R. A.; Gajiwala, K. S.; He, M.; Hogan, R. J.; Kozminski, K.; Li, L. Y.; Lockner, J. W.; Lou, J.; Marra, M. T.; Mitchell, L. J., Jr.; Murray, B. W.; Nieman, J. A.; Noell, S.; Planken, S. P.; Rowe, T.; Ryan, K.; Smith, G. J., III.; Solowiej, J. E.; Steppan, C. M.; Taggart, B. Discovery of ketone-based covalent inhibitors of coronavirus 3CL proteases for the potential therapeutic treatment of COVID-19. *J. Med. Chem.* **2020**, *63*, 12725–12747.

(41) Carreira, E. M.; Fessard, T. C. Four-membered ring-containing spirocycles: synthetic strategies and opportunities. *Chem. Rev.* **2014**, *114*, 8257–8322.

(42) Talele, T. T. Opportunities for tapping into three-dimensional chemical space through a quaternary carbon. *J. Med. Chem.* **2020**, *63*, 13291–13315.

(43) Zheng, Y.; Tice, C. M.; Singh, S. B. The use of spirocyclic scaffolds in drug discovery. *Bioorg. Med. Chem. Lett.* **2014**, *24*, 3673–3682.

(44) Ghosh, A. K.; Duong, T. T.; McKee, S. P.; Thompson, W. J. N. N'-Disuccinimidyl carbonate: A useful reagent for alkoxy-carbonylation of amines. *Tetrahedron Lett.* **1992**, *33*, 2781–2784.

(45) Kjell, D. P.; Slattery, B. J.; Semo, M. J. A novel, nonaqueous method for regeneration of aldehydes from bisulfite adducts. *J. Org. Chem.* **1999**, *64*, 5722–5724.

(46) He, X.; Quan, S.; Xu, M.; Rodriguez, S.; Goh, S. L.; Wei, J.; Fridman, A.; Koepflinger, K. A.; Carroll, S. S.; Grobler, J. A.; Espeseth, A. S.; Olsen, D. B.; Hazudas, D. J.; Wang, D. Generation of SARS-CoV-2 reporter replicon for high-throughput antiviral screening and testing. *Proc. Natl. Acad. Sci. U.S.A.* **2021**, *118*, No. e2025866118.

(47) Pirali, T.; Serafini, M.; Cargnin, S.; Genazzani, A. A. Applications of deuterium in medicinal chemistry. *J. Med. Chem.* **2019**, *62*, 5276–5297.

(48) Kabsch, W. Automatic indexing of rotation diffraction patterns. *J. Appl. Crystallogr.* **1988**, *21*, 67–72.

(49) Kabsch, W. XDS. *Acta Crystallogr., Sect. D: Struct. Biol.* **2010**, *66*, 125–132.

(50) Vonrhein, C.; Flensburg, C.; Keller, P.; Sharff, A.; Smart, O.; Paciorek, W.; Womack, T.; Bricogne, G. Data processing and analysis with the autoPROC toolbox. *Acta Crystallogr., Sect. D: Biol. Crystallogr.* **2011**, *67*, 293–302.

(51) Evans, P. R. An introduction to data reduction: space-group determination, scaling and intensity statistics. *Acta Crystallogr., Sect. D: Biol. Crystallogr.* **2011**, *67*, 282–292.

(52) McCoy, A. J.; Grosse-Kunstleve, R. W.; Adams, P. D.; Winn, M. D.; Storoni, L. C.; Read, R. J. Phaser crystallographic software. *J. Appl. Crystallogr.* **2007**, *40*, 658–674.

(53) Adams, P. D.; Afonine, P. V.; Bunkóczi, G.; Chen, V. B.; Davis, I. W.; Echols, N.; Headd, J. J.; Hung, L.-W.; Kapral, G. J.; Grosse-Kunstleve, R. W.; PHENIX: a comprehensive Python-based system for macromolecular structure solution. *Acta Crystallogr., Sect. D: Biol. Crystallogr.* **2010**, *66*, 213–221.

(54) Emsley, P.; Lohkamp, B.; Scott, W. G.; Cowtan, K. Features and development of Coot. *Acta Crystallogr., Sect. D: Biol. Crystallogr.* **2010**, *66*, 486–501.

(55) Chen, V. B.; Arendall, W. B.; Headd, J. J.; Keedy, D. A.; Immormino, R. M.; Kapral, G. J.; Murray, L. W.; Richardson, J. S.; Richardson, D. C. MolProbity: all-atom structure validation for macromolecular crystallography. *Acta Crystallogr., Sect. D: Biol. Crystallogr.* **2010**, *66*, 12–21.

(56) Potterton, L.; McNicholas, S.; Krissinel, E.; Gruber, J.; Cowtan, K.; Emsley, P.; Murshudov, G. N.; Cohen, S.; Perrakis, A.; Noble, M. Developments in the CCP4 molecular-graphics project. *Acta Crystallogr., Sect. D: Biol. Crystallogr.* **2004**, *60*, 2288–2294.

(57) Evans, P. Scaling and assessment of data quality. *Acta Crystallogr., Sect. D: Biol. Crystallogr.* **2006**, *62*, 72–82.

(58) Diederichs, K.; Karplus, P. A. Improved R-factors for diffraction data analysis in macromolecular crystallography. *Nat Struct Biol.* **1997**, *4*, 269–275.

(59) Weiss, M. S. Global indicators of X-ray data quality. *J. Appl. Crystallogr.* **2001**, *34*, 130–135.

(60) Karplus, P. A.; Diederichs, K. Linking crystallographic model and data quality. *Science* **2012**, *336*, 1030–1033.

(61) Evans, P. Biochemistry. Resolving some old problems in protein crystallography. *Science* **2012**, *336*, 986–987.

(62) Sacco, M. D.; Ma, C.; Lagarias, P.; Gao, A.; Townsend, J. A.; Meng, X.; Dube, P.; Zhang, X.; Hu, Y.; Kitamura, N.; Hurst, B.; Tarbet, B.; Marty, M. T.; Kolocouris, A.; Xiang, Y.; Chen, Y.; Wang, J. Structure and inhibition of the SARS-CoV-2 main protease reveal strategy for developing dual inhibitors against M(pro) and cathepsin L. *Sci. Adv.* **2020**, *6*, No. eabe0751.

(63) Kim, Y.; Gaudreault, N.; Meekins, D. A.; Perera, K.; Bold, D.; Trujillo, J. D.; Morozov, I.; McDowell, C. D.; Chang, K. O.; Richt, R. A. Effects of Spike Mutations in SARS-CoV-2 variants of concern on human or animal ACE2-mediated virus entry and neutralization. *bioRxiv* **2021**, No. 457627.